

GEORCE: A Fast New Control Algorithm for Computing Geodesics

Frederik Möbius Rygaard^{1*} and Søren Hauberg^{1*}

^{1*}DTU Compute, Technical University of Denmark (DTU), Anker Engelundsvej 1, Kongens Lyngby, 2800, Denmark.

*Corresponding author(s). E-mail(s): fmry@dtu.dk; sohau@dtu.dk;

Abstract

Computing geodesics for Riemannian manifolds is a difficult task that often relies on numerical approximations. However, these approximations tend to be either numerically unstable, have slow convergence, or scale poorly with manifold dimension and number of grid points. We introduce a new algorithm called *GEORCE* that computes geodesics in a local chart via a transformation into a discrete control problem. We show that *GEORCE* has global convergence and quadratic local convergence. In addition, we show that it extends to Finsler manifolds. For both Finslerian and Riemannian manifolds, we thoroughly benchmark *GEORCE* against several alternative optimization algorithms and show empirically that it has a much faster and more accurate performance for a variety of manifolds, including key manifolds from information theory and manifolds that are learned using generative models.

Keywords: Riemannian Manifolds, Finsler Manifolds, Geodesics, Optimization, Control Problem

Mathematics Subject Classification 53C22, 49Q99, 65D15

1 Introduction

Reliably computing geodesics that connect point pairs is a constant source of frustration to practitioners working with non-trivial Riemannian manifolds. Such manifolds see common use across many fields, including medical image analysis [1–3], protein modeling [4–6], robotics [7–10], generative modeling [11–16] and information geometry [17–21].

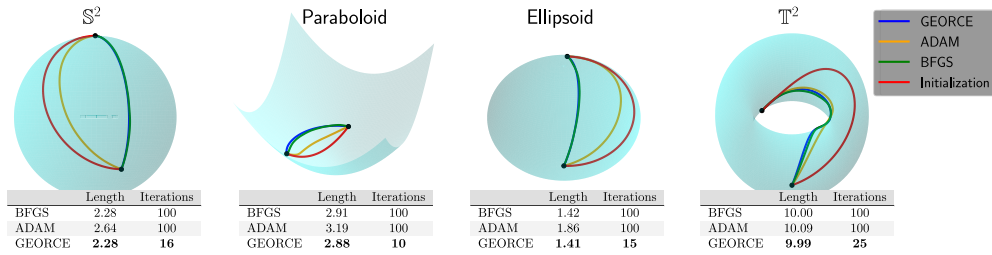


Fig. 1 Comparison between *GEORCE* and baseline methods for computing locally length minimizing geodesics between given point pairs on four different manifolds. All algorithms are terminated if the ℓ^2 -norm of the gradient of the discretized energy functional (5) is less than 10^{-4} , or the number of iterations exceeds 100. Note that sometimes the respective solutions overlap, making it difficult to distinguish them. Also note, that in the case of the torus the initial curve determines the direction around the hole so that the obtained geodesics follow this direction and are therefore clearly not the globally shortest geodesics between the given start and end point. Experimental details and benchmark data are in Appendix F.

Geodesics, or *locally shortest paths*, are the key computational tools for engaging with data residing on a Riemannian manifold. The lengths of geodesic curves inform us about manifold distances. Likewise, the *exponential* and *logarithm maps*, which generalize vector addition and subtraction, are rooted in geodesics [22, Chapter 9]. Unfortunately, the solution to the boundary-value problem for geodesics are only available in closed form for the simplest manifolds, and numerical approximations are therefore required in practice.

Such approximations are typically achieved by minimizing the *energy functional* over a suitable set of curves connecting the given boundary points and parametrized by $\gamma : [0, 1] \rightarrow U$ [23, Page 194]

$$\mathcal{E}(\gamma) = \frac{1}{2} \int_0^1 \dot{\gamma}(t)^\top G(\gamma(t)) \dot{\gamma}(t) dt, \quad (1)$$

where G denotes the metric matrix function of the manifold in local coordinates in a chart $\phi : U \rightarrow \mathcal{M}$, where U is an open subset of \mathbb{R}^d . This energy is commonly minimized with general-purpose gradient-based optimization methods [11, 12, 24] or, in particular when considering the initial value problem and using shooting methods, by solving the system of ordinary differential equations that arise by applying the Euler-Lagrange equations [25, 26]. Unfortunately, both approaches are often numerically brittle, exhibit slow convergence, or scale poorly with the number of grid points and manifold dimensions.

In this paper, we introduce the *GEORCE* algorithm (*GEodesic Optimization algoRithm using Control tEchniques*) that computes numerical solutions to the geodesic boundary value problem via an optimal control strategy. *GEORCE* applies to general Riemannian as well as general Finslerian manifolds. We show that the algorithm has global convergence similar to gradient descent and that it has quadratic local convergence similar to the Newton method. Empirically, we compare *GEORCE* with alternative optimization algorithms on the discretized energy functional and see

that *GEORCE* is much faster and attains lower Riemannian length as illustrated in Fig. 1.

2 Background and related work

A **Riemannian manifold**, (\mathcal{M}, g) , can indirectly be considered as a smooth n -dimensional surface in a Euclidean space of sufficiently high dimension, see [27, 28]. In this way \mathcal{M} inherits its metric g from the ambient space. All the intrinsic geometry of (\mathcal{M}, g) , including curvature and geodesic distances, are encoded in the metric g . The metric can be – and often is – constructed independently of the formal embedding alluded to above, namely directly as a symmetric positive definite matrix valued function on the domain of a parametrization of the manifold in question. The metric, $g : T_x\mathcal{M} \times T_x\mathcal{M} \rightarrow \mathbb{R}$, defines an inner product that smoothly varies over the tangent spaces of \mathcal{M} such that in a local chart $g(v, w) = v^\top G(x)w$, where G is the metric matrix function evaluated in $x \in \mathcal{M}$ for $v, w \in T_x\mathcal{M}$. The tangent space, $T_x\mathcal{M}$, consists of tangents to all curves at $x \in \mathcal{M}$ [23, Page 7 Definition 2.6].

A **geodesic** can then be defined using the inner product in each tangent space. The length of a curve, $\gamma : [0, 1] \rightarrow U$ parameterized by $t \in [0, 1]$ is given by

$$\mathcal{L}(\gamma) = \int_0^1 \sqrt{\dot{\gamma}(t)^\top G(\gamma(t))\dot{\gamma}(t)} dt, \quad (2)$$

where $\phi : U \rightarrow \mathcal{M}$ is a local chart for an open set $U \subset \mathbb{R}^d$. A Riemannian manifold can be equipped with a unique metrically compatible connection, ∇ , known as the Levi-Civita Connection [23, Page 55 Theorem 3.6], where uniqueness and existence are guaranteed by completeness of the metric [23, Page 63 Lemma 2.3]. Note that curves are geodesics if and only if they are critical points of the energy functional, i.e., the first variation of the energy functional is zero for all variations with fixed endpoints assuming that the end points are not conjugate points [23, Page 196 Proposition 2.5]. This also holds in the Finslerian case [29, Page 81].

An equivalent way to define geodesics is to define these as curves, γ , with zero acceleration using the Levi-Civita connection as the covariant derivative, i.e., $\nabla_{\dot{\gamma}(t)}\dot{\gamma}(t) = 0$. In a local chart, this gives rise to the following (usually non-linear) ODE-system [23, Page 62]

$$\frac{d^2\gamma^k}{dt^2} + \Gamma_{ij}^k \frac{d\gamma^i}{dt} \frac{d\gamma^j}{dt} = 0, \quad \gamma(0) = a, \gamma(1) = b, \quad (3)$$

written in Einstein notation¹, where $\{\Gamma_{ij}^k\}_{i,j,k}$ denote the Christoffel symbols. The exponential map $\text{Exp}_x(v) : T_x\mathcal{M} \rightarrow \mathcal{M}$ is then defined as $\text{Exp}_x(v) = \gamma(1)$, where γ is a geodesic with $\gamma(0) = x \in \mathcal{M}$ and initial velocity vector, $v \in T_x\mathcal{M}$, i.e. $\dot{\gamma}(0) = v$. Within the injectivity radius of x the exponential map, Exp_x , is a diffeomorphism and its inverse is the logarithmic map, $\text{Log}_x : \mathcal{M} \rightarrow T_x\mathcal{M}$.

¹In Einstein notation, upper and lower indices constitute a sum, i.e. $a^i b_i = \sum_i a_i b_i$

Examples of Riemannian manifolds include information geometric spaces, i.e., statistical manifolds, where “points” in the manifold correspond to statistical distributions. These can be equipped with the so-called Fisher-Rao metric, see [18, 30]:

$$G_{ij}(\theta) = \int_{\mathcal{X}} p(x|\theta) \left(\frac{\partial}{\partial \theta^i} \log p(x|\theta) \right) \left(\frac{\partial}{\partial \theta^j} \log p(x|\theta) \right) d\mu(x), \quad (4)$$

where θ corresponds to the parameters of the probability density function p under a measure μ . Informally, the Fisher-Rao metric can be seen as a measure of the amount of information in the data around a parameter θ [31].

The energy functional in Eq. 1 can be discretized and minimized using standard optimization methods. Consider fixed start and end points $x_0 = a \in U$ and $x_T = b \in U$, and let $x_{0:T} := \{x_t\}_{t=0}^T$ denote a discretized version of the candidate curve γ in $T + 1$ points in a local chart U . Minimizing the energy functional can be rewritten as a discrete constrained optimization problem, i.e., subdivision of $[0, 1]$ into T subintervals, in the chosen local chart [11, 12]

$$E(x_{0:T}) = \min_{x_{0:T}} \sum_{t=0}^{T-1} (x_{t+1} - x_t)^\top G(x_t) (x_{t+1} - x_t) \quad (5)$$

s.t. $x_0 = a, x_T = b,$

where $G(\cdot)$ denotes the metric matrix function in local coordinates, and the tangent vectors of the coordinate expression for γ are discretized as $\dot{\gamma}(t) \approx (x_{t+1} - x_t) T$. Note that the constant scaling by $1/2$ is omitted since it does not affect the optimal solution. With this formulation, the curve is approximated as a piece-wise linear function. This is not restrictive since γ can be approximated into a curve for any given precision T or converted to a smooth function, e.g., using splines [24]. Note that by approximating the functional energy by forward differences, the computational error is linear in $1/T$, that is, in the form $\mathcal{O}(1/T)$.

Similarly to the energy functional in Eq. 1, it is assumed that a stationary point to the discretized energy functional in Eq. 5 is either a local or global minimum point. Thus, the number of points, T , in Eq. 5 needs to be sufficiently high to achieve this. If this is not fulfilled, then there may exist saddle points for the discretized energy functional.

The optimization problem in Eq. 5 can be solved using standard solvers in the variables $x_{1:(T-1)}$. Gradient descent converges to a local minimum (*global convergence*), but will have local linear convergence, while a Newton method or quasi-Newton method will have local

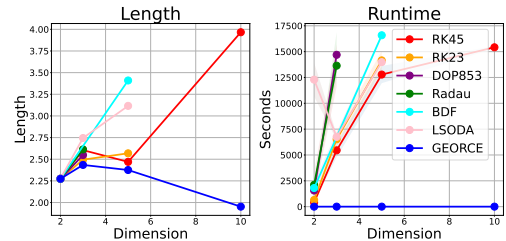


Fig. 2 The estimates of BVP-solvers with different integration methods compared to *GEORCE* on \mathbb{S}^n for $n = 2, 3, 5, 10$. The BVP-solvers minimize the squared error to the boundary condition using *BFGS* [32–35]. All methods are terminated if they take more than 24 hours or use more than 10 GB of memory on a CPU. Details on the experiment is found in Appendix F.1.

quadratic and super-linear convergence, respectively, but will involve solving a linear equation system and will, in general, not have global convergence [36, Chapter 8].

Limitations of existing numerical solvers. Solving the ODE-system in Eq. 3 as a boundary value problem (BVP) can have difficulties converging depending on the choice of initial velocity vector [25] and does not scale well in higher dimension. We illustrate this in Fig. 2, where we show the estimated length and runtime for \mathbb{S}^n with $n = 2, 3, 5, 10, 20$ for different integration methods compared to our proposed algorithm (*GEORCE*). Different approaches try to circumvent this by solving the BVP on subintervals [25, 37] or solving the BVP-problem as a fixed-point problem in a probabilistic manner [38, 39]. However, these methods often require access to higher-order information about the metric tensor, e.g in the form of Christoffel symbols.

Directly minimizing the energy in Eq. 5 can, e.g., be done using off-the-shelf solvers like *ADAM* [40] or *BFGS* [32–35]. However, these methods tend to have slow convergence and scale poorly in the manifold dimension and number of grid points (see Sec. 5). Alternatively, the geodesic can be estimated by discretizing the smooth manifold by simplicial complexes [41], for which there exist different geodesic solvers [42–46]. Although discretized manifolds appear naturally in computational geometry, the approach is not scalable to discretize high-dimensional smooth manifolds.

3 GEORCE

To develop an efficient primal-dual algorithm for computing geodesics, we will first reformulate the discretized energy functional (5) as a discrete control problem in a local chart. We then derive the necessary conditions for a minimum for the control problem using techniques from optimal control to decompose the discrete control problem into strictly convex subproblems; from this, we deduce an iterative scheme to compute geodesics. Finally, we prove that our proposed algorithm exhibits global convergence and local quadratic convergence.

We will assume the following for our algorithm

- We assume access to a local chart of the manifold and assume that the entire candidate curve of the geodesic can be represented within the same chart.
- All computations are performed within the local coordinate chart U , which is defined based on the induced metric of the Riemannian manifold.
- For computational efficiency, we will leverage the Euclidean properties of the local chart (i.e., straight-line interpolation within U).
- We will assume that the end points are not conjugate points, and that the discretization is sufficiently fine such that a critical point of the discretized energy functional in Eq. 5 is either a local or global minimum point.

3.1 Derivation of GEORCE

As a starting point, we reformulate the problem of finding a minimum of the discrete energy functional (5) to a control problem in a local chart

$$\begin{aligned} \min_{(x_{1:T-1}, u_{0:T-1})} \quad & \left\{ \sum_{t=0}^{T-1} u_t^\top G(x_t) u_t \right\} \\ \text{s.t.} \quad & x_{t+1} = x_t + u_t, \quad t = 0, \dots, T-1, \\ & x_0 = a, x_T = b. \end{aligned} \tag{6}$$

Here, $x_{0:T}$ denotes the state variables, while $u_{0:(T-1)}$ corresponds to the control variables, i.e., the velocity vectors along the curve (modulo scaling). A key insight into our approach is that rephrasing into an optimal control problem leads to a set of convex subproblems. Using this, we derive the following proposition.

Proposition 1 *The necessary conditions for a minimum in Eq. 6 is*

$$\begin{aligned} 2G(x_t)u_t + \mu_t &= 0, \quad t = 0, \dots, T-1, \\ x_{t+1} &= x_t + u_t, \quad t = 0, \dots, T-1, \\ \nabla_y \left[u_t^\top G(y)u_t \right] \Big|_{y=x_t} + \mu_t &= \mu_{t-1}, \quad t = 1, \dots, T-1. \\ x_0 &= a, x_T = b, \end{aligned} \tag{7}$$

where $\mu_t \in \mathbb{R}^d$ for $t = 0, \dots, T-1$.

Proof The Hamiltonian of Eq. 6 is

$$H_t(x_t, u_t, \mu_t) = u_t^\top G(x_t)u_t + \mu_t^\top (x_t + u_t).$$

The Hamiltonian $H_t(x_t, u_t, \mu_t)$ is strictly convex in u_t , since $G(x_t)$ is positive definite. The time-discrete version of Pontryagin's maximum principle [47] then yields the following when applied to our control problem (6)

$$\begin{aligned} 2G(x_t)u_t + \mu_t &= 0, \quad t = 0, \dots, T-1, \\ x_{t+1} &= x_t + u_t, \quad t = 0, \dots, T-1, \\ \nabla_y \left[u_t^\top G(y)u_t \right] \Big|_{y=x_t} + \mu_t &= \mu_{t-1}, \quad t = 1, \dots, T-1. \\ x_0 &= a, x_T = b. \end{aligned} \tag{8}$$

□

Proposition 1 decomposes the minimization problem in Eq. 6 into a system of equations for each time step t . Note that these equations are necessary conditions for the optimum for Eq. 6 and are sufficient in the case where the objective function in Eq. 6 is convex in both x_t and u_t [48, Page 244]. However, this is generally not the case, but due to the assumption applying a sufficiently fine discretization the solution to Eq. 7 will be a local or global minimum point.

The problem with the necessary conditions in Proposition 1 is that the equations cannot be solved in closed form for a general metric matrix function, G . To circumvent this, we will derive an iterative scheme. Consider the variables $x_{0:T}^{(i)}$ and $u_{0:T}^{(i)}$ in iteration i . We apply the “trick” of fixing the metric matrix function, and the derivative of the inner product in iteration i .

$$\begin{aligned}\nu_t &:= \nabla_y (u_t^\top G(y) u_t) \Big|_{y=x_t^{(i)}, u_t=u_t^{(i)}}, \quad t = 1, \dots, T-1, \\ G_t &:= G(x_t^{(i)}), \quad t = 0, \dots, T-1,\end{aligned}\tag{9}$$

Fixing these in iteration i , the system of equations in Eq. 7 reduces to

$$\begin{aligned}2G_t u_t + \mu_t &= 0, \quad t = 0, \dots, T-1, \\ \nu_t + \mu_t &= \mu_{t-1}, \quad t = 1, \dots, T-1, \\ \sum_{t=0}^{T-1} u_t &= b - a,\end{aligned}\tag{10}$$

where $\nu_{1:(T-1)}$ and $G_{0:(T-1)}$ are fixed (9). Since $G_{0:(T-1)}$ are positive definite, the modified system of equations in Eq. 10 can be explicitly solved in iteration i for $u_{0:(T-1)}$ and $\mu_{0:(T-1)}$ as shown in the following proposition.

Proposition 2 *The update scheme for u_t, μ_t and x_t is*

$$\begin{aligned}\mu_{T-1} &= \left(\sum_{t=0}^{T-1} G_t^{-1} \right)^{-1} \left(2(a - b) - \sum_{t=0}^{T-1} G_t^{-1} \sum_{t>j}^{T-1} \nu_j \right), \\ u_t &= -\frac{1}{2} G_t^{-1} \left(\mu_{T-1} + \sum_{j>t}^{T-1} \nu_j \right), \quad t = 0, \dots, T-1, \\ x_{t+1} &= x_t + u_t, \quad t = 0, \dots, T-1, \\ x_0 &= a.\end{aligned}\tag{11}$$

Proof From the update formula $\nu_t + \mu_t = \mu_{t-1}$ for $t = 1, \dots, T-1$ we deduce that $\mu_t = \mu_{T-1} + \sum_{j>t}^{T-1} \nu_j$. From the update scheme $2G_t u_t + \mu_t = 0$ we deduce that $u_t = -\frac{1}{2} G_t^{-1} \mu_t$, since G_t is positive definite and hence has a well-defined inverse. Noting that $\sum_{t=0}^{T-1} u_t = b - a$

we can re-write the iterative formulas as

$$\begin{aligned}\mu_t &= \mu_{T-1} + \sum_{j>t}^{T-1} \nu_j, \quad t = 0, \dots, T-1, \\ u_t &= -\frac{1}{2} G_t^{-1} \left(\mu_{T-1} + \sum_{j>t}^{T-1} \nu_j \right), \quad t = 0, \dots, T-1, \\ -\frac{1}{2} \sum_{t=0}^{T-1} G_t^{-1} \left(\mu_{T-1} + \sum_{j>t+1}^{T-1} \nu_j \right) &= b - a.\end{aligned}$$

The last equation can be used to solve for μ_{T-1} utilizing that the sum of (inverse) positive definite matrices is positive definite and has a well-defined inverse

$$\mu_{T-1} = \left(\sum_{t=0}^{T-1} G_t^{-1} \right)^{-1} \left(2(a-b) - \sum_{t=0}^{T-1} G_t^{-1} \sum_{t>j}^{T-1} \nu_j \right),$$

which proves the result. \square

Algorithm 1 GEORCE for Riemannian manifolds

- 1: **Input:** tol, T
- 2: **Output:** Geodesic estimate $x_{0:T}$
- 3: Set $x_t^{(0)} \leftarrow a + \frac{b-a}{T}t$, $u_t^{(0)} \leftarrow \frac{b-a}{T}$ for $t = 0, \dots, T$ and $i \leftarrow 0$
- 4: **while** $\left\| \nabla_y E(y) \Big|_{y=x_t^{(i)}} \right\|_2 > \text{tol}$ **do**
- 5: $G_t \leftarrow G \left(x_t^{(i)} \right)$ for $t = 0, \dots, T-1$
- 6: $\nu_t \leftarrow \nabla_y \left(u_t^{(i)} G(y) u_t^{(i)} \right) \Big|_{y=x_t^{(i)}}$ for $t = 1, \dots, T-1$
- 7: $\mu_{T-1} \leftarrow \left(\sum_{t=0}^{T-1} G_t^{-1} \right)^{-1} \left(2(a-b) - \sum_{t=0}^{T-1} G_t^{-1} \sum_{t>j}^{T-1} \nu_j \right)$
- 8: $\tilde{u}_t \leftarrow -\frac{1}{2} G_t^{-1} \left(\mu_{T-1} + \sum_{j>t}^{T-1} \nu_j \right)$ for $t = 0, \dots, T-1$
- 9: Using line search find α^* for the following optimization problem with the discrete energy functional E

$$\begin{aligned}\alpha^* &= \arg \min_{\alpha} E(\tilde{x}_{0:T}) \quad (\text{exact line search}) \\ \text{s.t.} \quad \tilde{x}_{t+1} &= \tilde{x}_t + \alpha \tilde{u}_t + (1-\alpha)u_t^{(i)}, \quad t = 0, \dots, T-1, \\ \tilde{x}_0 &= a.\end{aligned}$$

- 10: Set $u_t^{(i+1)} \leftarrow \alpha^* \tilde{u}_t + (1-\alpha^*)u_t^{(i)}$ for $t = 0, \dots, T-1$
 - 11: Set $x_{t+1}^{(i+1)} \leftarrow x_t^{(i+1)} + u_t^{(i+1)}$ for $t = 0, \dots, T-1$
 - 12: $i \leftarrow i+1$
 - 13: **end while**
 - 14: return x_t for $t = 0, \dots, T-1$
-

Proposition 2 immediately leads to an iterative update of $(x_t^{(i)}, u_t^{(i)})$ to estimate the geodesic, which we denote the *GEORCE*-algorithm. *GEORCE* is described in pseudo-code in Algorithm 1. Since the computations in *GEORCE* take place in a local chart, it is implicitly assumed that the computations are well-defined within the chart. Let $\phi : U \rightarrow \mathcal{M}$ denote the chart, where $U \subseteq \mathbb{R}^d$ is an open set. It is assumed that the initialization of the curve in Algorithm 1 is defined within the chart, i.e., $x_t^{(0)} \in U$ for all t . If the updated solution $\tilde{x} \notin U$ in iteration $i + 1$, then soft line-search (see below) is applied to determine a point in U on the line between $(x^{(i)}, u^{(i)})$ and (\tilde{x}, \tilde{u}) , since U is an open set. Note also that if the computations of *GEORCE* are close to the boundary of U , one can change the chart assuming overlapping charts in the atlas of the manifold. Thus, in practice, it is not a problem for *GEORCE* if U is only a subset of \mathbb{R}^d . For all computations in this paper, we will not change chart or assume that we can leave the domain U during the computations, but such cases can easily be modified into the algorithm as described above.

As we show below, *GEORCE* exhibits global convergence, which means that the algorithm will converge to a local minimum. If there are multiple local minima, then *GEORCE* will not necessarily find the global minimum. To investigate whether *GEORCE* has found the global minimum, one can apply *GEORCE* for different initial curves to compute locally-length minimizing curves and choose the curve with the shortest length as the global minimum. In Appendix C, we illustrate the effect of different choices of initialization curves and how it affects the solution using *GEORCE*.

Line search and stopping criteria

We find that an appropriate step size is necessary to ensure global convergence for *GEORCE* (See Proposition 5), and therefore we update $u_t^{(i+1)} \leftarrow \alpha u_t^{(i+1)} + (1 - \alpha)u_t^{(i)}$ in iteration i . Here, α denotes the step size, which we estimate with line search. One approach is to estimate the optimal step size in each iteration, but, in our experience, this is unnecessarily expensive. We instead use *soft* line search, which merely ensures that the objective function decreases in each iteration [36]. We implement this using backtracking, where an initial step size is multiplied by a decay rate, $0 < \rho < 1$, until some condition is met, e.g., the Wolfe condition [49], the Armijo condition [50], or the curvature condition² [49]. In practice, we find that the Armijo condition [50] with $\rho = 0.5$ is sufficient for most manifolds, although the decay rate can be fine-tuned to increase the performance of *GEORCE*.

We threshold the ℓ^2 -norm of the gradient of the discrete energy functional as a stopping criteria for *GEORCE*. In all empirical comparisons, identical stopping criteria are applied to all optimization algorithms.

Comparison with other optimization methods

GEORCE has complexity $\mathcal{O}(Td^3)$ due to matrix inversions along the discretized curve but scales only linearly in T , unlike e.g. quasi-Newton methods (Table 1). Although the computational complexity in the manifold dimension is of a lower order for quasi-Newton methods and gradient descent, *GEORCE* exhibits faster convergence. Since

²Note that the term “curvature condition” is rather misleading in a Riemannian context as it refers to conditions on the derivative of the objective function and not the Riemannian curvature.

| Algorithm | Global convergence | Local convergence | Gradient | Hessian | Complexity |
|------------------|--------------------|-------------------|----------|---------|-----------------------|
| Gradient descent | ✓ | Linear | ✓ | ✗ | $\mathcal{O}(Td^2)$ |
| Quasi-Newton | ✗ | Super linear | ✓ | ✗ | $\mathcal{O}(T^2d^2)$ |
| Newton method | ✗ | Quadratic | ✓ | ✓ | $\mathcal{O}(Td^3)$ |
| GEORCE | ✓ | Quadratic | ✓ | ✗ | $\mathcal{O}(Td^3)$ |

Table 1 Convergence, complexity, and use of higher order derivatives for different optimization algorithms in each iteration, where T is the number of grid points and d is the manifold dimension. A checkmark indicates that the algorithm exhibits the property, while a cross indicates that it is not the case.

the Hessian of the discretized energy functional in Eq. 5 is sparse, the update step in the Newton method can be simplified in complexity compared to the standard Newton method that has complexity $\mathcal{O}(T^3d^3)$ (see Appendix B.2). However, the sparse Newton step requires second-order derivatives, unlike *GEORCE*, which only requires first-order derivatives of the discretized energy. Note that in Table 1, we assume that the iterations for the different methods remain well-defined in the chosen chart.

3.2 Convergence results

In this section, we show that *GEORCE* exhibits global convergence, i.e., converges to a local minimum, and that *GEORCE* exhibits local quadratic convergence under certain regularity of the discretized energy functional. To simplify the notation, we let $\langle \cdot, \cdot \rangle$, $\|\cdot\|$ and ∇ denote the Euclidean inner product, norm and gradient in \mathbb{R}^d , respectively.

Global convergence

We will prove that *GEORCE* converges to a (local) minimum. To prove this, we will use the fact that the discretized energy functional is smooth and hence locally Lipschitz. This implies that the first order Taylor approximation of the discretized energy functional can be written as

$$\Delta E = \langle \nabla E(z_0), \Delta z \rangle + \mathcal{O}(\Delta z) \|\Delta z\|, \quad (12)$$

Thus, the term $\mathcal{O}(\Delta z) \|\Delta z\|$ can be re-written as $\mathcal{O}(\|\Delta z\|^2)$ locally.

To prove global convergence for the algorithm *GEORCE* we first show existence and uniqueness by proving two lemmas. Secondly, we prove that in each iteration the discretized energy functional is decreasing, unless a (local) minimum has been found.

For notation set $x^{(i)} = (a, x_1^{(i)}, \dots, x_{T-1}^{(i)}, b)$ and $u^{(i)} = (u_0^{(i)}, u_1^{(i)}, \dots, u_{T-2}^{(i)}, u_{T-1}^{(i)})$ as the solution for iteration i such that $(x^{(i+1)}, u^{(i+1)})$ is the solution using the update scheme in proposition 2.

Lemma 3 *Assume that $(x^{(i)}, u^{(i)})$ is a feasible solution, then*

1. *There exists a unique solution $(x^{(i+1)}, u^{(i+1)})$ to the system of equations in Eq. 11 based on $(x^{(i)}, u^{(i)})$.*
2. *All linear combinations $(1 - \alpha)(x^{(i)}, u^{(i)}) + \alpha(x^{(i+1)}, u^{(i+1)})$ for $0 < \alpha \leq 1$ are feasible solutions.*

Proof Since the matrices, $\{G(x_t^{(i)})\}_{t=0}^T$ are positive definite, then the matrices are regular with unique inverse, and so are the sum of the inverse matrices. This means that there exists a unique solution to the update scheme in proposition 2 proving 1.

Initially, assume that $(x^{(i+1)}, u^{(i+1)})$ is well-defined in the local chart.

Since the solution $(x^{(i+1)}, u^{(i+1)})$ is also a feasible solution for the update scheme in proposition 2, then the linear combination of two feasible solutions will also be a feasible solution, i.e.

$$\sum_{t=0}^{T-1} u_t^{(j)} = (b - a), \quad j = 1, \dots, (i + 1).$$

The new solution based on the linear combination gives

$$\begin{aligned} (1 - \alpha) \sum_{t=0}^{T-1} u_t^{(i)} + \alpha \sum_{t=0}^{T-1} u_t^{(i+1)} &= (1 - \alpha)(b - a) + \alpha(b - a) = (b - a) \\ (1 - \alpha)x^{(i)} + \alpha x^{(i+1)} &= (1 - \alpha) \left(\alpha, x_1^{(i)}, \dots, x_{T-1}^{(i)}, b \right) + \alpha \left(a, x_1^{(i+1)}, \dots, x_{T-1}^{(i+1)}, b \right) \\ &= \left(a, (1 - \alpha)x_1^{(i)} + \alpha x_1^{(i+1)}, \dots, (1 - \alpha)x_{T-1}^{(i)} + \alpha x_{T-1}^{(i+1)}, b \right), \end{aligned}$$

where for any $t = 0, \dots, T - 1$

$$\begin{aligned} (1 - \alpha)x_t^{(i)} + \alpha x_t^{(i+1)} &= (1 - \alpha) \left(a + \sum_{j=0}^{t-1} u_j^{(i)} \right) + \alpha \left(a + \sum_{j=0}^{t-1} u_j^{(i+1)} \right) \\ &= a + \sum_{j=0}^{t-1} \left((1 - \alpha)u_j^{(i)} + \alpha u_j^{(i+1)} \right). \end{aligned}$$

This shows that the linear combination in the state is feasible as it produces feasible state variables in terms of start and end point. Furthermore, each state variable is feasible, if they were determined from the linear combination of the control vectors, which proves that the linear combinations of the state and control variables are also feasible solutions.

If $(x^{(i+1)}, u^{(i+1)})$ is not well-defined in the local chart, then the line-search in *GEORCE* will be able to determine a point belonging to the manifold and that will be on the line between $(x^{(i+1)}, u^{(i+1)})$ and $(x^{(i)}, u^{(i)})$ as the local chart is defined on an open set and $x^{(i)}$ is well-defined in the local chart. The new solution is then a feasible solution following the argument above. \square

Lemma 4 Let $\{x_t^{(i)}, u_t^{(i)}\}_{t=0}^T$ denote the feasible solution after iteration i in *GEORCE*.

If $\{x_t^{(i)}, u_t^{(i)}\}_{t=0}^T$ is not a (local) minimum point, then the feasible solution from iteration $\{x_t^{(i+1)}, u_t^{(i+1)}\}_{t=0}^T$ will decrease the objective function in the sense that there exists an $\eta > 0$ such that for all α with $0 < \alpha \leq \eta \leq 1$, then

$$E \left(x^{(i)} + \alpha \left(x^{(i+1)} - x^{(i)} \right), u^{(i)} + \alpha \left(u^{(i+1)} - u^{(i)} \right) \right) < E \left(x^{(i)}, u^{(i)} \right),$$

where $x^{(i)} = \left(a, x_1^{(i)}, \dots, x_{T-1}^{(i)}, b \right)$ and $u^{(i)} = \left(u_0^{(i)}, u_1^{(i)}, \dots, u_{T-2}^{(i)}, u_{T-1}^{(i)} \right)$.

Proof $E(x, u)$ is a smooth function. The first order Taylor approximation of the energy function $E(x, u)$ in Eq. 5 in (x, u) is

$$\begin{aligned} \Delta E(x, u) &= \sum_{t=1}^{T-1} \left(\left\langle \nabla_{x_t} E(x_t, u_t) \Big|_{(x_t, u_t) = (x_t^{(i)}, u_t^{(i)})}, \Delta x_t \right\rangle + \mathcal{O}(\Delta x_t) \|\Delta x_t\| \right) \\ &\quad + \sum_{t=0}^{T-1} \left(\left\langle \nabla_{u_t} E(x_t, u_t) \Big|_{(x_t, u_t) = (x_t^{(i)}, u_t^{(i)})}, \Delta u_t \right\rangle + \mathcal{O}(\Delta u_t) \|\Delta u_t\| \right), \end{aligned}$$

where $\Delta u_t := u_t^{(i+1)} - u_t^{(i)}$ and $\Delta x_t := x_t^{(i+1)} - x_t^{(i)}$. By the optimality conditions in Eq. 7 we have that

$$\begin{aligned} \nabla_{x_t} E(x, u) \Big|_{(x, u) = (x_t^{(i)}, u_t^{(i)})} &= \mu_{t-1} - \mu_t, \quad t = 1, \dots, T-1, \\ \nabla_{u_t} E(x, u) \Big|_{(x_t, u_t) = (x_t^{(i)}, u_t^{(i+1)})} &= -\mu_t, \quad t = 0, \dots, T-1. \end{aligned} \tag{13}$$

Inserting the optimality conditions in the Taylor expansion we have that

$$\begin{aligned} \Delta E(x, u) &= \sum_{t=1}^{T-1} \left(\langle \mu_{t-1} - \mu_t, \Delta x_t \rangle + \mathcal{O}(\Delta x_t) \|\Delta x_t\| \right) \\ &\quad + \sum_{t=0}^{T-1} \left(\left\langle \nabla_{u_t} E(x, u) \Big|_{(x, u) = (x_t^{(i)}, u_t^{(i)})}, \Delta u_t \right\rangle + \mathcal{O}(\Delta u_t) \|\Delta u_t\| \right). \end{aligned}$$

Since $\Delta x_t = \sum_{j=0}^{t-1} \Delta u_j$, then

$$\begin{aligned} \Delta E(x, u) &= \sum_{t=1}^{T-1} \left(\left\langle \mu_{t-1} - \mu_t, \sum_{j=0}^{t-1} \Delta u_j \right\rangle + \mathcal{O} \left(\sum_{j=0}^{t-1} \Delta u_j \right) \left\| \sum_{j=0}^{t-1} \Delta u_j \right\| \right) \\ &\quad + \sum_{t=0}^{T-1} \left(\left\langle \nabla_{u_t} E(x, u) \Big|_{(x, u) = (x_t^{(i)}, u_t^{(i)})}, \Delta u_t \right\rangle + \mathcal{O}(\Delta u_t) \|\Delta u_t\| \right). \end{aligned}$$

Re-arranging the terms we get

$$\begin{aligned} \Delta E(x, u) &= \sum_{t=0}^{T-2} \left\langle \mu_t, \sum_{j=0}^t \Delta u_j \right\rangle \\ &\quad - \sum_{t=1}^{T-1} \left(\left\langle \mu_t, \sum_{j=0}^{t-1} \Delta u_j \right\rangle + \mathcal{O} \left(\sum_{j=0}^{t-1} \Delta u_j \right) \left\| \sum_{j=0}^{t-1} \Delta u_j \right\| \right) \\ &\quad + \sum_{t=0}^{T-1} \left(\left\langle \nabla_{u_t} E(x_t, u_t) \Big|_{(x_t, u_t) = (x_t^{(i)}, u_t^{(i)})}, \Delta u_t \right\rangle + \mathcal{O}(\Delta u_t) \|\Delta u_t\| \right) \\ &= \langle \mu_0, \Delta u_0 \rangle + \sum_{t=1}^{T-2} \langle \mu_t, \Delta u_t \rangle - \left\langle \mu_{T-1}, \sum_{j=0}^{T-1} \Delta u_j \right\rangle + \langle \mu_{T-1}, \Delta u_{T-1} \rangle \\ &\quad + \sum_{t=0}^{T-1} \left(\left\langle \nabla_{u_t} E(x_t, u_t) \Big|_{(x_t, u_t) = (x_t^{(i)}, u_t^{(i)})}, \Delta u_t \right\rangle + \mathcal{O}(\Delta u_t) \|\Delta u_t\| \right) \end{aligned}$$

Since $\Delta u_j = u_j^{(i+1)} - u_j^{(i)}$ and $\Delta x_j = x_j^{(i+1)} - x_j^{(i)}$ for $j = 0, \dots, T$, and since the solution is feasible we have that $\sum_{j=0}^{T-1} u_j^{(i)} = b - a$ for any i , which implies that $\sum_{j=0}^{T-1} \Delta u_j = 0$. This

reduces the above expression to

$$\begin{aligned}
\Delta E(x, u) &= \sum_{t=0}^{T-1} \left(\langle \mu_t, \Delta u_t \rangle + \mathcal{O} \left(\sum_{j=0}^{t-1} \Delta u_j \right) \left\| \sum_{j=0}^{t-1} \Delta u_j \right\| \right) \\
&\quad + \sum_{t=0}^{T-1} \left(\left\langle \nabla_{u_t} E(x_t, u_t) \Big|_{(x_t, u_t) = (x_t^{(i)}, u_t^{(i)})}, \Delta u_t \right\rangle + \mathcal{O}(\Delta u_t) \|\Delta u_t\| \right) \\
&= \sum_{t=0}^{T-1} \left\langle \mu_t + \nabla_{u_t} E(x, u) \Big|_{(x, u) = (x_t^{(i)}, u_t^{(i)})}, \Delta u_t \right\rangle \\
&\quad + \sum_{t=0}^{T-1} \mathcal{O} \left(\sum_{j=0}^{t-1} \Delta u_j \right) \left\| \sum_{j=0}^{t-1} \Delta u_j \right\| + \sum_{t=0}^{T-1} \mathcal{O}(\Delta u_t) \|\Delta u_t\|.
\end{aligned}$$

By Eq. 13 we have

$$\begin{aligned}
\mu_t + \nabla_{u_t} E(x_t, u_t) \Big|_{(x_t, u_t) = (x_t^{(i)}, u_t^{(i)})} &= -\nabla_{u_t} E(x_t, u_t) \Big|_{(x_t, u_t) = (x_t^{(i)}, u_t^{(i+1)})} \\
&\quad + \nabla_{u_t} E(x, u) \Big|_{(x, u) = (x_t^{(i)}, u_t^{(i)})} \\
&= -2G(x_t^{(i)}) (u_t^{(i+1)} - u_t^{(i)}),
\end{aligned} \tag{14}$$

which implies that

$$\begin{aligned}
\Delta E(x, u) &= \sum_{t=0}^{T-1} \left\langle -2G(x_t^{(i)}) \Delta u_t, \Delta u_t \right\rangle \\
&\quad + \sum_{t=0}^{T-1} \left(\mathcal{O} \left(\sum_{j=0}^{t-1} \Delta u_j \right) \left\| \sum_{j=0}^{t-1} \Delta u_j \right\| + \mathcal{O}(\Delta u_t) \|\Delta u_t\| \right).
\end{aligned} \tag{15}$$

Since $G(x_t^{(i)})$ is positive definite, the first summation is negative assuming that at least one non-zero vector $\{\Delta u_t\}_{t=0}^{T-1}$, which is the case, since we have assumed that $(x_t^{(i)}, u_t^{(i)})$ is not a (local) minimum. Now scale all vectors, $\{\Delta u_t\}_{t=0}^{T-1}$ with a scalar $0 < \alpha < 1$. Note that the term, $-2G(x_t^{(i)}) \Delta u_t$, is unaffected by this, since it equals $\mu_t + \nabla_{u_t} E(x, u) (x_t^{(i)}, u_t^{(i)})$, which is independent of α . The first order Taylor order approximation is

$$\begin{aligned}
\Delta E(x, u) &= \sum_{t=0}^{T-1} \left\langle -2G(x_t^{(i)}) \Delta u_t, \alpha \Delta u_t \right\rangle \\
&\quad + \sum_{t=0}^{T-1} \left(\mathcal{O} \left(\sum_{j=0}^{t-1} \alpha \Delta u_j \right) \left\| \sum_{j=0}^{t-1} \alpha \Delta u_j \right\| + \mathcal{O}(\alpha \Delta u_t) \|\alpha \Delta u_t\| \right).
\end{aligned}$$

In the limit it now follows that there exists an $\eta > 0$ such that $\frac{\Delta E(x, u)}{\alpha} < 0$ for some α with $0 < \alpha \leq \eta \leq 1$, which implies that $\Delta E(x, u) < 0$. \square

Proposition 5 *Let $E^{(i)}$ be the value of the discretized energy functional for the solution after iteration i (with line search) in GEORCE. If the starting point $(x^{(0)}, u^{(0)})$ is feasible, then the series $\{E^{(i)}\}_{i>0}$ will converge to a (local) minimum.*

Proof If the starting point $(x^{(0)}, u^{(0)})$ in *GEORCE* is feasible, then the points $(x^{(i)}, u^{(i)})$ after each iteration (with line-search) in *GEORCE* will also be feasible solutions by lemma 3.

The discretized energy functional is a positive function, i.e. a lower bound is at least 0. Assume that the series $\{E^{(i)}\}_{i>0}$ is not converging to a (local) minimum. From lemma 4 it follows that $\{E^{(i)}\}_{i>0}$ is decreasing for increasing i , and since $E^{(i)}$ has a lower bound, the series $\{E^{(i)}\}_i$ can not be non-converging. Assume now that the convergence value for $\{E^{(i)}\}_i$, denoted \hat{E} , is not a (local) minimum, and denote the convergence point (\hat{x}, \hat{u}) . According to lemma 4 *GEORCE* will from the solution (\hat{x}, \hat{u}) in the following iteration produce a new point (\tilde{x}, \tilde{u}) such that $E(\tilde{x}, \tilde{u}) < \hat{E}$, which is contradiction as the series $\{E^{(i)}\}_i$ is assumed to be converging to \hat{E} . The series, $\{E^{(i)}\}_i$, will therefore converge, and the convergence point is a (local) minimum. \square

It is not possible for *GEORCE* to jump between two local minimum points. To see this, assume that there are two local minimum points that have the same discretized energy, and assume that *GEORCE* is jumping between the two points, i.e., there is convergence to a local minimum in terms of the discretized energy functional according to Proposition 5, but not to a single local minimum point. In the *GEORCE* iteration, the line search will try to improve the discretized energy functional by finding a point closer to one of the two minimum points. Either this leads to a new point with improved discretized energy, or *GEORCE* stops concluding that a local minimum point has been found since no improvements in discretized energy were possible by line-search in accordance with Lemma 4. But this contradicts the assumption that *GEORCE* jumps between two minimum points with the same discretized energy. Thus, *GEORCE* converges to only one local minimum point.

Local convergence

We will show that *GEORCE* under certain regularity of the discretized energy functional exhibits local convergence in the sense that

$$\exists \epsilon > 0 : \exists c > 0 : \forall z^{(i)} \in B_\epsilon(z^*) : \|z^{(i+1)} - z^*\| \leq c \|z^{(i)} - z^*\|^2, \quad (16)$$

for some $c > 0$. We will assume the following regularity of the discretized energy functional

Assumption 6 (Local convergence) *We assume the following regarding the discretized energy functional.*

- *We assume that the discretized energy functional $E(z)$ is locally strictly convex in the (local) minimum point $z^* = (x^*, u^*)$ in the sense that*

$$\exists \epsilon > 0 : \forall z \in B_\epsilon(z^*), z \neq z^* : \forall \alpha \in]0, 1[: E((1 - \alpha)z + \alpha z^*) < (1 - \alpha)E(z) + \alpha E(z^*),$$

where $B_\epsilon = \{z \mid \|z - z^*\| < \epsilon\}$.

- Assume that the discretized energy functional $E(z)$ is smooth, and consider the first order Taylor approximation of the discretized energy functional

$$\Delta E = \langle \nabla E(z_0), \Delta z \rangle + \mathcal{O}(\Delta z) \|\Delta z\|,$$

Then, the term $\mathcal{O}(\Delta z) \|\Delta z\|$ can be re-written as $\mathcal{O}(\|\Delta z\|^2)$ locally.

Intuitively, it is expected that *GEORCE* exhibits local quadratic convergence. *GEORCE* solves iteratively quadratic minimization problems by fixing the metric matrix function. Since *GEORCE* exhibits global convergence, the metric matrix function in each iteration of *GEORCE* will converge to the metric matrix function at the local minimum. Close to the local minimum, the metric matrix function will be approximately constant, since it is smooth and hence continuous. At that point, *GEORCE* is simply solving a quadratic optimization problem, which is solved in one iteration similar to the Newton method, i.e., has quadratic convergence. It is therefore expected that when *GEORCE* is sufficiently close to the minimum a large “dip” will occur. This is especially clear for the Euclidean space, where $G = I$ is independent of x . Therefore, *GEORCE* will find the exact solution after one iteration, as it simply solves a quadratic minimization problem. We illustrate the convergence of *GEORCE* and the baseline algorithms for \mathbb{S}^2 and \mathbb{R}^2 in Fig. 3. We first prove the following result, before proving quadratic local convergence.

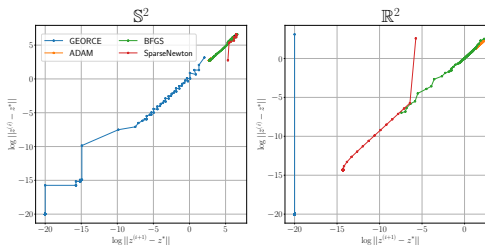


Fig. 3 Illustration of the convergence of *GEORCE* and baseline algorithms. We plot $\log \|z^{(i)} - z^*\|$ over $\log \|z^{(i+1)} - z^*\|$ for each iteration i for the different methods. We use the convergence point of *GEORCE* as z^* . If the norms are 0, we set the value to -20 . All initial curves are set to the same random deformation of a straight line similar to Appendix C.

Lemma 7 Assume $f(x)$ is a smooth function. Let z^* be a (local) minimum point for f , and assume that f is locally strictly convex in z^* . Then

$$\exists \epsilon > 0 : \quad \forall z \in B_\epsilon(z^*) \setminus \{z^*\} : \quad \langle \nabla f(z), z^* - z \rangle < 0.$$

Proof Since f is locally strictly convex in z^* , it follows that

$$\exists \epsilon > 0 : \quad \forall z \in B_\epsilon(z^*), z \neq z^* : \quad \forall \alpha \in]0, 1[: \quad f((1 - \alpha)z + \alpha z^*) < (1 - \alpha)f(z) + \alpha f(z^*),$$

which implies that

$$\exists \epsilon > 0 : \quad \forall z \in B_\epsilon(z^*) : \quad \forall \alpha \in]0, 1[: \quad \frac{f(z + \alpha(z^* - z)) - f(z)}{\alpha} < f(z^*) - f(z).$$

As f is locally strictly convex in the minimum point z^*

$$\exists \epsilon > 0 : \quad \forall z \in B_\epsilon(z^*), z \neq z^* : \quad f(z^*) - f(z) < 0,$$

which follows from the fact that if there exists a $z' \in B_\epsilon(z^*)$ with $f(z') = f(z^*)$, then since f is locally strictly convex in z^* , then

$$\forall \alpha \in]0, 1[: \quad (1 - \alpha)f(z') + \alpha f(z^*) = f(z^*) > f((1 - \alpha)z + \alpha z^*).$$

However, this contradicts that z' and z^* are local minimum points. Since f is a smooth function, then the first order Taylor approximation gives

$$\frac{f(z + \alpha(z^* - z)) - f(z)}{\alpha} = \langle \nabla f(z), z^* - z \rangle + \mathcal{O}(\alpha(z^* - z)) \|z^* - z\| < f(z^*) - f(z) < 0.$$

In the limit, then $\lim_{\alpha \searrow 0} \mathcal{O}(\alpha(z^* - z)) = 0$, which implies that $\langle \nabla f(z), z^* - z \rangle < 0$. \square

Proposition 8 *If the discretized energy functional is locally strictly convex in the (local) minimum point z^* and locally $\alpha^* = 1$, i.e. no line search, then GEORCE has locally quadratic convergence, i.e.*

$$\exists \epsilon > 0 : \quad \exists c > 0 : \quad \forall z^{(i)} \in B_\epsilon(z^*) : \quad \|z^{(i+1)} - z^*\| \leq c \|z^{(i)} - z^*\|^2,$$

where $z^{(i)} = (x^{(i)}, u^{(i)})$ is the solution from GEORCE at iteration i .

Proof Assume that z^* is a (local) minimum point. Since GEORCE has global convergence to a (local) minimum point by theorem 5, we will assume that the algorithm has convergence point $E(z^*)$. Consider iteration i with $z^{(i)} = (x^{(i)}, u^{(i)})$ from GEORCE, and assume that all following iterations in GEORCE are in the ball $B_{\epsilon_1}(z^*)$, and fulfill the locally strictly convex assumption in 6. Note that as the series $\{z^{(i)}\}$ converges to z^* , then $\{z^{(i)}\}_{i \geq k} \subset B_{\epsilon_1}(z^*)$ for some $k > 0$. It follows as $E(z)$ is locally Lipschitz continuous that

$$E(z^{(i+1)} - z^*) - E(z^*) = \mathcal{O}(\|z^{(i+1)} - z^*\|),$$

since $z^{(i+1)} \in B_\epsilon(z^*)$. The left hand term above can be rearranged into

$$E(z^{(i+1)}) - E(z^*) = (E(z^{(i+1)}) - E(z^{(i)})) + (E(z^{(i)}) - E(z^*)).$$

By Eq. 15 in the proof of lemma 4 and utilizing $\alpha^* = 1$, it follows that

$$\begin{aligned}
& E(z^{(i+1)}) - E(z^*) \\
&= \left(E(z^{(i+1)}) - E(z^{(i)}) \right) + \left(E(z^{(i)}) - E(z^*) \right) \\
&= \sum_{t=0}^{T-1} \left(\langle -2G(x_t^{(i)}) \Delta u_t, \Delta u_t \rangle + \mathcal{O} \left(\sum_{j=0}^{t-1} \Delta u_j \right) \left\| \sum_{j=0}^{t-1} \Delta u_j \right\| + \mathcal{O}(\Delta u_t) \|\Delta u_t\| \right) \\
&\quad - \sum_{t=0}^{T-1} \langle -2G(x_t^{(i)}) \Delta u_t, (u_t^* - u_t^{(i)}) \rangle \\
&\quad - \mathcal{O} \left(\sum_{j=0}^{t-1} (u_j^* - u_j^{(i)}) \right) \left\| \sum_{j=0}^{t-1} (u_j^* - u_j^{(i)}) \right\| - \mathcal{O}(u_t^* - u_t^{(i)}) \|u_t^* - u_t^{(i)}\| \\
&= \sum_{t=0}^{T-1} \left(\langle -2G(x_t^{(i)}) \Delta u_t, \Delta u_t - (u_t^* - u_t^{(i)}) \rangle + \mathcal{O} \left(\sum_{j=0}^{t-1} \Delta u_j \right) \left\| \sum_{j=0}^{t-1} \Delta u_j \right\| \right) \\
&\quad + \sum_{t=0}^{T-1} \left(\mathcal{O}(\Delta u_t) \|\Delta u_t\| + \mathcal{O} \left(\sum_{j=0}^{t-1} (u_j^* - u_j^{(i)}) \right) \left\| \sum_{j=0}^{t-1} (u_j^* - u_j^{(i)}) \right\| \right) \\
&\quad + \sum_{t=0}^{T-1} \left(\mathcal{O}(u_t^* - u_t^{(i)}) \|u_t^* - u_t^{(i)}\| \right) \\
&= \sum_{t=0}^{T-1} \left(\langle 2G(x_t^{(i)}) \Delta u_t, u_t^* - u_t^{(i+1)} \rangle + \mathcal{O} \left(\sum_{j=0}^{t-1} \Delta u_j \right) \left\| \sum_{j=0}^{t-1} \Delta u_j \right\| \right) \\
&\quad + \sum_{t=0}^{T-1} \mathcal{O}(\Delta u_t) \|\Delta u_t\| \\
&\quad + \sum_{t=0}^{T-1} \left(\mathcal{O} \left(\sum_{j=0}^{t-1} (u_j^* - u_j^{(i)}) \right) \left\| \sum_{j=0}^{t-1} (u_j^* - u_j^{(i)}) \right\| + \mathcal{O}(u_t^* - u_t^{(i)}) \|u_t^* - u_t^{(i)}\| \right).
\end{aligned}$$

Observe now that the term $2G(x_t^{(i)}) \Delta u_t$ is the gradient for $z_t^{(i)}$. Define ϵ_2 such that the \mathcal{O} -terms are sufficiently close to zero for all $z \in B_{\epsilon_2}(z^*)$. Thus, for $\epsilon = \min\{\epsilon_1, \epsilon_2\}$ we have from lemma 7

$$\sum_{t=0}^{T-1} \langle 2G(x_t^{(i)}) \Delta u_t, u_t^* - u_t^{(i+1)} \rangle < 0,$$

since E is assumed locally strictly convex in the local minimum point z^* by assumptions 6. Combining the inequalities and utilizing that $E(z)$ is locally Lipschitz continuous by assumptions 6, then

$$\mathcal{O} \left(\|z^{(i+1)} - z^*\| \right) = E(z^{(i+1)}) - E(z^*) \leq \mathcal{O} \left(\|z^{(i)} - z^*\|^2 \right),$$

which implies that there exists an $\epsilon > 0$ such that

$$\forall z^{(i)} \in B_\epsilon(z^*) : \quad \|z^{(i+1)} - z^*\| \leq c \|z^{(i)} - z^*\|^2,$$

for $c > 0$. □

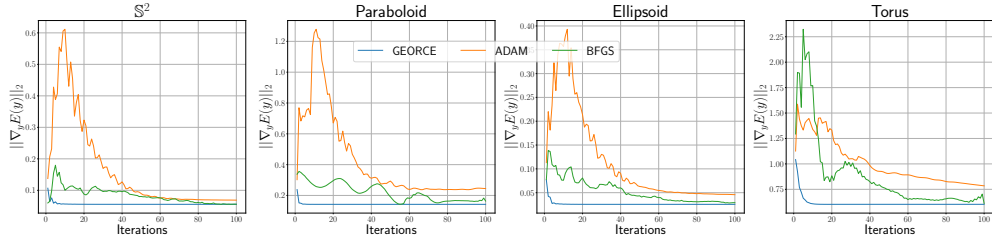


Fig. 4 The figure shows the ℓ^2 -norm of the gradient of Eq. 5 for each iteration for *GEORCE* and alternative methods applied to construct geodesics for 100 iterations for four different manifolds corresponding to Fig. 1. We see that the ℓ^2 -norm of the gradient of Eq. 5 for *GEORCE* converges considerably faster than for alternative algorithms.

The assumption in the above proof that the line search parameter, $\alpha^* = 1$ locally at the minimum point is based on that locally the approximation of the discretized energy functional becomes close to the true function.

Fig. 4 shows the convergence by plotting the ℓ^2 -norm of the gradient of the discretized energy functional in each iteration for four different manifolds. Note that by formulating the geodesic boundary problem as a control problem, we estimate the discretized tangent vectors along the curve $\{u_t\}_{t=0}^T$. Modulo scaling u_0 will in the limit of a sufficiently fine grid correspond to the logarithmic map, $\text{Log}_a b$.

4 Extension to Finslerian geometry

A Finsler geometry can be seen as a generalization of Riemannian geometry, where the tangent spaces are not equipped with a quadratic form metric but with a Finsler metric instead. A Finsler metric, $F : \mathcal{M} \times T\mathcal{M} \rightarrow \mathbb{R}_+$, where \mathcal{M} is a differentiable manifold, is a Minkowski norm in the sense that F is C^∞ on $T\mathcal{M} \setminus \{0\}$, $F(x, cv) = cF(x, v)$ for all $v \in T\mathcal{M}$, $x \in \mathcal{M}$ and $c > 0$ and for any $v \in T\mathcal{M}$, then $\frac{\partial^2 F}{\partial v^i \partial v^j}(x, v)$ is positive definite [29, Chapter 2]. Geodesics for a Finsler manifold can be found equivalently to the Riemannian case by minimizing the energy functional, $\int_0^1 F^2(\gamma(t), \dot{\gamma}(t)) dt$, on a suitable set of curves connecting the two points thereby approximating a geodesic γ , [29, Chapter 3]. In this way, the indicatrix field for Finslerian manifolds consists of non-centered ellipses unlike the Riemannian case, meaning that the distance is not symmetric for Finslerian manifolds. We illustrate this in Fig. 5 for the local chart for the sphere used in Fig. 1, where we shift the indicatrix fields by a wind-field on the form $(0, 0.75)$.

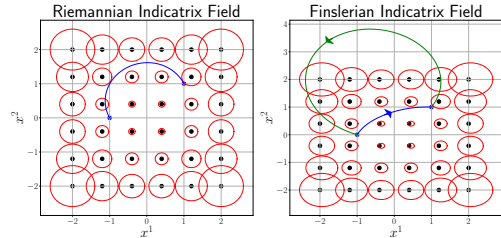


Fig. 5 The red circles shows the indicatrix field, $\{v \in T_x\mathcal{M} \mid F(x, v) = 1\}$, in the chart of the sphere used in the Riemannian case in Fig. 1 and its corresponding center is marked with black dot. The left figure is the Riemannian case, while the right figure is the Finslerian case corresponding to a force field making the indicatrix-field become non-centered ellipsis for the geodesics (blue and green), where the arrow indicates the direction of the curve.

GEORCE is similarly applicable to Finsler geometry. First, we note that the energy functional can be written as [29, Page 20]

$$\frac{1}{2} \int_0^1 F^2(\gamma(t), \dot{\gamma}(t)) dt = \int_0^1 \dot{\gamma}(t)^\top G(\gamma(t), \dot{\gamma}(t)) \dot{\gamma}(t) dt, \quad (17)$$

where $G(x, v) = \frac{1}{2} \frac{\partial^2 F^2}{\partial v^i \partial v^j}(x, v)$ denotes the fundamental tensor in local coordinates³, which is positive definite [29, Page 19]. Unlike the Riemannian case, the fundamental tensor, G , is now a function of both the position and velocity, which implies the update formulas in Proposition 2. Similar to Riemannian case, we can formulate the discrete energy functional for the Finsler case as the following discretized energy functional in Eq. 17 becomes

$$E_F(x_{0:T}) := \min_{x_{0:T}} \sum_{t=0}^{T-1} (x_{t+1} - x_t)^\top G(x_t, x_{t+1} - x_t) (x_{t+1} - x_t) \quad (18)$$

s.t. $x_0 = a, x_T = b,$

where the corresponding discrete control problem becomes

$$\min_{(x_{1:T-1}, u_{0:T-1})} \sum_{t=0}^{T-1} u_t^\top G(x_t, u_t) u_t, \quad t = 0, \dots, T-1, \quad (19)$$

s.t. $x_{t+1} = x_t + u_t$
 $x_0 = a, x_T = b,$

Since, the fundamental tensor, G , depends on both the state, $x_{0:T}$, and control variable $u_{0:T}$, the necessary conditions in Proposition 1 have to be modified slightly to take this into account. Taking this into account and following the same approach as in the Riemannian case, we get the following update scheme in the Finslerian case (see Appendix A.1 for details)

$$\mu_{T-1} = \left(\sum_{t=0}^{T-1} G_t^{-1} \right)^{-1} \left(2(a-b) - \sum_{t=0}^{T-1} G_t^{-1} \left(\zeta_t + \sum_{t>j}^{T-1} \nu_j \right) \right),$$

$$u_t = -\frac{1}{2} G_t^{-1} \left(\mu_{T-1} + \zeta_t + \sum_{j>t}^{T-1} \nu_j \right), \quad t = 0, \dots, T-1, \quad (20)$$

$x_{t+1} = x_t + u_t, \quad t = 0, \dots, T-1,$
 $x_0 = a,$

³In literature, the fundamental tensor is often denoted with a lower case g . To have the notation consistent with the Riemannian case, we opt to use an upper case G instead.

where in iteration i we fix

$$\begin{aligned}\nu_t &:= \nabla_y (u_t^\top G(y, u_t) u_t) \Big|_{y=x_t^{(i)}, u_t=u_t^{(i)}}, \quad t = 1, \dots, T-1, \\ \zeta_t &:= \nabla_y (u_t^\top G(x_t, y) u_t) \Big|_{x_t=x_t^{(i)}, u_t=u_t^{(i)}, y=u_t^{(i)}}, \quad t = 1, \dots, T-1, \\ G_t &:= G(x_t^{(i)}, u_t^{(i)}), \quad t = 0, \dots, T-1.\end{aligned}$$

We see that the only extra term in *GEORCE* for Finsler manifolds is $\{\zeta_t\}_{t=0}^{T-1}$. Using the modified update scheme in Eq. 20, we estimate geodesics for Finsler manifolds similar to Algorithm 1. For completeness, we show the algorithm in pseudo-code for the Finsler case in Appendix B.1.

Using the same technique as in the Riemannian case, we show that *GEORCE* for Finsler manifolds has global convergence and local quadratic convergence. We refer to the details in Appendix A.2.

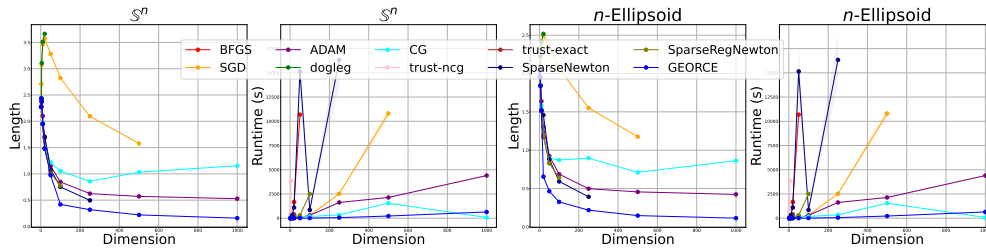


Fig. 6 The first two figures display the length and runtime of geodesics for \mathbb{S}^n estimated using different algorithms from Table 2. The latter row shows the length and runtime, respectively, for the n -Ellipsoid with half axes of n equally spaced points between 0.5 and 1.0. The optimization solvers are described in Appendix F.1.

5 Experiments

Riemannian manifolds

To compare *GEORCE* with other optimization algorithms, we show the runtime and length of the geodesics computed for different manifolds with varying dimensions in Table 2 on a CPU. In Table 3 and Table 4, we show the corresponding results on a GPU for compatible methods for $T = 100$ and $T = 50$, respectively. Here we compare *GEORCE* with *BFGS* [32–35] and *ADAM* [40]. We terminate the algorithm if the ℓ^2 -norm of the gradient of the discretized energy functional in Eq. 5 is less than 10^{-4} , or if the number of iterations exceeds 1,000. A full description of the manifolds and experimental details can be found in Appendix D and Appendix F, respectively.

We show the estimated geodesics with $T = 100$ grid points and summarize the results for the corresponding runtime and length of the computed geodesics for the n -sphere and n -ellipsoid in Fig. 6. In general, we see that *GEORCE* is considerably faster with a shorter length compared to alternative methods.

To test *GEORCE* on manifolds with multiple length minimizing geodesics, we consider the geodesic between $(-5, -5)$ and $(5, 5)$ on an “egg-tray” parameterized by $(x, y, 2 \cos x \cos y)$ with $T = 1,000$ grid points. We show the estimates in Fig. 7, where we see that *GEORCE* obtains a significantly smaller length, where there is also a clear symmetry to solution to *GEORCE* along the other side of the “egg-tops”.

To illustrate the application of *GEORCE* to more abstract manifolds, we compute geodesics on the statistical manifolds, i.e., between distributions [17, 18]. Fig. 8 shows

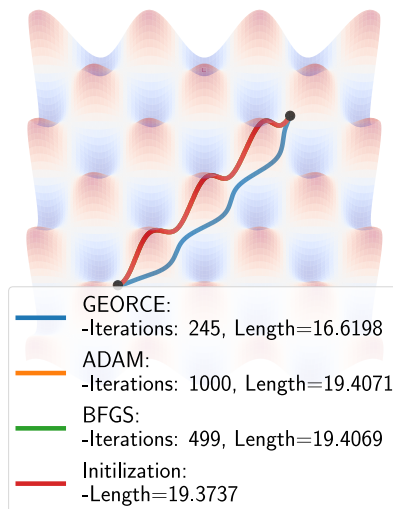


Fig. 7 The geodesics for an “egg-tray” parameterized by $(x, y, 2 \cos x \cos y)$, where there are no unique geodesic connecting the points. The *BFGS* estimate, *ADAM* estimate and the initial curve overlap completely.

| Riemannian Manifold | BFGS (T=100) | | | ADAM (T=100) | | | GEORCE (T=100) | | |
|-----------------------|---------------|---------------------------|--------|-------------------------|---------------|------------------------|----------------|------------------------|--|
| | Length | Runtime | Length | Runtime | Length | Runtime | Length | Runtime | |
| \mathbb{S}^2 | 2.2742 | 57.4164 ± 0.0616 | 2.2772 | 0.2335 ± 0.0005 | 2.2741 | 0.0078 ± 0.0000 | 2.2741 | 0.0078 ± 0.0000 | |
| \mathbb{S}^3 | 2.4342 | 67.4657 ± 0.4874 | 2.4377 | 0.3475 ± 0.0010 | 2.4342 | 0.0635 ± 0.0001 | 2.4342 | 0.0635 ± 0.0001 | |
| \mathbb{S}^5 | 2.3757 | 77.6975 ± 0.0741 | 2.4222 | 1.9894 ± 0.0188 | 2.3755 | 0.2219 ± 0.0001 | 2.3755 | 0.2219 ± 0.0001 | |
| \mathbb{S}^{10} | 1.9529 | 150.0621 ± 0.8919 | 2.1016 | 4.4208 ± 0.0308 | 1.9523 | 0.3184 ± 0.0002 | 1.9523 | 0.3184 ± 0.0002 | |
| \mathbb{S}^{20} | 1.4810 | 1068.8645 ± 17.2001 | 1.6839 | 8.7097 ± 0.0352 | 1.4808 | 0.6732 ± 0.0204 | 1.4808 | 0.6732 ± 0.0204 | |
| \mathbb{S}^{50} | 1.0464 | 7350.6001 ± 244.3737 | 1.1463 | 61.8926 ± 0.3034 | 0.9749 | 4.1016 ± 0.0201 | 0.9749 | 4.1016 ± 0.0201 | |
| \mathbb{S}^{100} | — | — | 0.8466 | 277.4217 ± 0.2280 | 0.4187 | 10.9208 ± 0.0071 | 0.4187 | 10.9208 ± 0.0071 | |
| \mathbb{S}^{250} | — | — | 0.6244 | 1424.9031 ± 22.1592 | 0.3192 | 78.2937 ± 0.0091 | 0.3192 | 78.2937 ± 0.0091 | |
| \mathbb{S}^{500} | — | — | 0.5717 | 2242.4697 ± 17.9769 | 0.2198 | 224.2761 ± 0.4894 | 0.2198 | 224.2761 ± 0.4894 | |
| \mathbb{S}^{1000} | — | — | 0.5279 | 4329.6621 ± 38.0163 | 0.1573 | 893.4682 ± 7.3130 | 0.1573 | 893.4682 ± 7.3130 | |
| E (2) | 1.9595 | 56.9650 ± 0.4106 | 1.9596 | 0.2328 ± 0.0001 | 1.9595 | 0.0067 ± 0.0001 | 1.9595 | 0.0067 ± 0.0001 | |
| E (3) | 2.0499 | 94.1769 ± 0.7044 | 2.0525 | 0.3392 ± 0.0024 | 2.0501 | 0.0119 ± 0.0000 | 2.0501 | 0.0119 ± 0.0000 | |
| E (5) | 1.8403 | 194.5403 ± 1.3293 | 1.9521 | 2.2227 ± 0.0186 | 1.8410 | 0.4220 ± 0.0038 | 1.8410 | 0.4220 ± 0.0038 | |
| E (10) | 1.5114 | 427.6278 ± 4.1044 | 1.6384 | 4.5697 ± 0.0541 | 1.5139 | 0.4566 ± 0.0016 | 1.5139 | 0.4566 ± 0.0016 | |
| E (20) | 1.1795 | 1669.2692 ± 10.2877 | 1.3049 | 9.4335 ± 0.0507 | 0.6548 | 1.9786 ± 0.0031 | 0.6548 | 1.9786 ± 0.0031 | |
| E (50) | 0.8338 | 10685.6133 ± 321.6447 | 0.9244 | 73.5682 ± 0.3306 | 0.4642 | 2.4208 ± 0.0222 | 0.4642 | 2.4208 ± 0.0222 | |
| E (100) | — | — | 0.6872 | 289.4196 ± 2.5224 | 0.3249 | 7.7128 ± 0.0714 | 0.3249 | 7.7128 ± 0.0714 | |
| E (250) | — | — | 0.4978 | 1620.6428 ± 16.9546 | 0.2178 | 56.8527 ± 0.1526 | 0.2178 | 56.8527 ± 0.1526 | |
| E (500) | — | — | 0.4559 | 2135.6899 ± 30.5699 | 0.1467 | 220.1656 ± 0.9902 | 0.1467 | 220.1656 ± 0.9902 | |
| E (1000) | — | — | 0.4232 | 4398.9453 ± 25.8738 | 0.1131 | 641.7199 ± 20.9901 | 0.1131 | 641.7199 ± 20.9901 | |
| \mathbb{T}^2 | 9.9851 | 92.7400 ± 3.1267 | 9.9855 | 0.1060 ± 0.0002 | 9.9851 | 0.0182 ± 0.0003 | 9.9851 | 0.0182 ± 0.0003 | |
| \mathbb{H}^2 | 1.2499 | 75.0079 ± 0.1710 | 1.2499 | 0.0988 ± 0.0001 | 1.2498 | 0.0025 ± 0.0001 | 1.2498 | 0.0025 ± 0.0001 | |
| \mathcal{P} (2) | 1.0669 | 88.2739 ± 0.4152 | 1.0879 | 0.2611 ± 0.0004 | 1.0669 | 0.0141 ± 0.0001 | 1.0669 | 0.0141 ± 0.0001 | |
| \mathcal{P} (3) | 2.2639 | 168.5082 ± 0.3039 | 2.2896 | 2.3780 ± 0.0046 | 2.2639 | 0.1442 ± 0.0002 | 2.2639 | 0.1442 ± 0.0002 | |
| Gaussian Distribution | 2.5952 | 47.6288 ± 0.1359 | 2.5956 | 0.0167 ± 0.0001 | 2.5952 | 0.0015 ± 0.0000 | 2.5952 | 0.0015 ± 0.0000 | |
| Fréchet Distribution | 1.1538 | 51.3063 ± 0.0566 | 1.1542 | 0.0185 ± 0.0001 | 1.1539 | 0.0009 ± 0.0000 | 1.1539 | 0.0009 ± 0.0000 | |
| Cauchy Distribution | 1.6454 | 36.5031 ± 0.0437 | 1.6466 | 0.0177 ± 0.0001 | 1.6452 | 0.0020 ± 0.0000 | 1.6452 | 0.0020 ± 0.0000 | |
| Pareto Distribution | 0.8297 | 39.0465 ± 0.0471 | 0.8336 | 0.0168 ± 0.0000 | 0.8297 | 0.0007 ± 0.0000 | 0.8297 | 0.0007 ± 0.0000 | |

Table 2 The length of the estimated geodesics for the *BFGS*-algorithm, *ADAM* and *GEORCE* on a CPU. The methods were terminated if the ℓ^2 -norm of the gradient was less than 10^{-4} or after 1,000 iterations. $E(n)$ denotes an Ellipsoid of dimension n with half axes of n equally spaced points between 0.5 and 1.0, while $\mathcal{P}(n)$ denotes the space of $n \times n$ symmetric positive definite matrices. When the computational time was longer than 24 hours, the value is set to —.

| Riemannian Manifold | ADAM (T=100) | | | Sparse Newton (T=100) | | | GEORCE (T=100) | | |
|-----------------------|---------------|------------------|--|-----------------------|-------------------|--|----------------|------------------------|--|
| | Length | Runtime | | Length | Runtime | | Length | Runtime | |
| S^2 | 2.2755 | 0.2729 ± 0.0016 | | 2.2742 | 0.1417 ± 0.0041 | | 2.2741 | 0.0163 ± 0.0003 | |
| S^3 | 2.4376 | 0.2890 ± 0.0005 | | 2.4342 | 0.2188 ± 0.0039 | | 2.4342 | 0.0735 ± 0.0018 | |
| S^5 | 2.4226 | 0.3153 ± 0.0027 | | 2.3755 | 0.8657 ± 0.0015 | | 2.3755 | 0.0494 ± 0.0014 | |
| S^{10} | 2.1031 | 0.3052 ± 0.0079 | | 1.9653 | 117.4589 ± 0.0140 | | 1.9523 | 0.0351 ± 0.0001 | |
| S^{20} | 1.6824 | 0.3401 ± 0.0117 | | 1.7069 | 146.3024 ± 0.0191 | | 1.4808 | 0.0483 ± 0.0020 | |
| S^{50} | 1.1456 | 0.5339 ± 0.0014 | | 1.0359 | 310.2160 ± 0.0200 | | 0.9749 | 0.0587 ± 0.0023 | |
| S^{100} | 0.8475 | 1.2935 ± 0.0014 | | 0.7522 | 6.6464 ± 0.0016 | | 0.4188 | 0.0717 ± 0.0022 | |
| S^{250} | 0.6251 | 3.8386 ± 0.0018 | | 0.4958 | 98.6502 ± 0.0147 | | 0.3192 | 0.3296 ± 0.0005 | |
| S^{500} | 0.5714 | 8.2031 ± 0.0030 | | 0.3787 | 899.4549 ± 0.0188 | | 0.2198 | 1.2925 ± 0.0003 | |
| S^{1000} | 0.5270 | 19.2234 ± 0.0712 | | — | — | | 0.1573 | 6.8579 ± 0.0023 | |
| $E(3)$ | 1.9595 | 0.2735 ± 0.0074 | | 1.9595 | 0.2177 ± 0.0075 | | 1.9595 | 0.0138 ± 0.0001 | |
| $E(5)$ | 2.0523 | 0.2839 ± 0.0056 | | 2.0498 | 0.3705 ± 0.0063 | | 2.0501 | 0.0167 ± 0.0001 | |
| $E(10)$ | 1.9594 | 0.2948 ± 0.0116 | | — | — | | 1.8410 | 0.0827 ± 0.0036 | |
| $E(20)$ | 1.6421 | 0.3097 ± 0.0133 | | 1.4247 | 116.6572 ± 0.0186 | | 1.5139 | 0.0547 ± 0.0019 | |
| $E(50)$ | 1.3052 | 0.3875 ± 0.0058 | | 1.4583 | 148.6781 ± 0.0307 | | 0.6514 | 0.1449 ± 0.0054 | |
| $E(100)$ | 0.9245 | 0.5704 ± 0.0013 | | 0.8849 | 316.9808 ± 0.0179 | | 0.4642 | 0.0370 ± 0.0014 | |
| $E(250)$ | 0.6873 | 1.3063 ± 0.0020 | | 0.5922 | 5.2868 ± 0.0007 | | 0.3249 | 0.0524 ± 0.0002 | |
| $E(500)$ | 0.4974 | 4.2084 ± 0.0029 | | 0.3917 | 84.6331 ± 0.0439 | | 0.2180 | 0.2325 ± 0.0001 | |
| $E(1000)$ | 0.4559 | 7.4772 ± 0.0024 | | 0.3039 | 827.7163 ± 0.1003 | | 0.1468 | 1.2897 ± 0.0004 | |
| \mathbb{T}^2 | 0.4238 | 19.8033 ± 0.0970 | | — | — | | 0.1129 | 5.1862 ± 0.0071 | |
| \mathbb{H}^2 | 9.9853 | 0.2890 ± 0.0016 | | 9.9851 | 0.3353 ± 0.0126 | | 9.9851 | 0.0549 ± 0.0010 | |
| $\mathcal{P}(2)$ | 1.2500 | 0.3201 ± 0.0004 | | 1.2498 | 0.2125 ± 0.0128 | | 1.2498 | 0.0089 ± 0.0003 | |
| $\mathcal{P}(3)$ | 1.0786 | 0.3801 ± 0.0047 | | 1.0669 | 0.2419 ± 0.0069 | | 1.0669 | 0.0227 ± 0.0010 | |
| Gaussian Distribution | 2.3006 | 0.4115 ± 0.0009 | | 2.3810 | 106.2814 ± 0.0135 | | 2.639 | 0.0343 ± 0.0004 | |
| Fréchet Distribution | 2.5951 | 0.1809 ± 0.0010 | | 2.5952 | 0.1108 ± 0.0055 | | 2.5952 | 0.0123 ± 0.0002 | |
| Cauchy Distribution | 1.1538 | 0.1778 ± 0.0029 | | 1.1539 | 0.0813 ± 0.0044 | | 1.1539 | 0.0055 ± 0.0003 | |
| Pareto Distribution | 1.6452 | 0.1818 ± 0.0007 | | 1.6453 | 0.1136 ± 0.0067 | | 1.6452 | 0.0137 ± 0.0001 | |
| | 0.8314 | 0.1779 ± 0.0026 | | 0.8297 | 0.0758 ± 0.0036 | | 0.8297 | 0.0043 ± 0.0002 | |

Table 3 The table shows the length of the estimated geodesics for different methods on a GPU. The methods have been stopped if the norm of the gradient was less than 10^{-4} or if a maximum of 1,000 iterations has been reached. When the computational time was longer than 24 hours, the value is set to —.

| Riemannian Manifold | ADAM (T=50) | | | Sparse Newton (T=50) | | | GEORCE (T=50) | | |
|-----------------------|-------------|----------------------|--|----------------------|-----------------------|--|---------------|---------------------------------------|--|
| | Length | Runtime | | Length | Runtime | | Length | Runtime | |
| S^2 | 2.2479 | 0.2683 ± 0.0082 | | 2.2478 | 0.1094 ± 0.0047 | | 2.2477 | 0.0187 ± 0.0002 | |
| S^3 | 2.4069 | 0.2593 ± 0.0110 | | 2.4064 | 0.1370 ± 0.0082 | | 2.4064 | 0.0866 ± 0.0031 | |
| S^5 | 2.3494 | 0.2907 ± 0.0103 | | 2.3480 | 0.3153 ± 0.0063 | | 2.3480 | 0.0622 ± 0.0019 | |
| S^{10} | 1.9470 | 0.3026 ± 0.0014 | | 1.9274 | 0.8966 ± 0.0034 | | 1.9272 | 0.0540 ± 0.0016 | |
| S^{20} | 1.5036 | 0.3349 ± 0.0069 | | 1.4610 | 28.7634 ± 0.0016 | | 1.4566 | 0.0670 ± 0.0003 | |
| S^{50} | 1.0320 | 0.4713 ± 0.0025 | | 1.0060 | 39.8257 ± 0.0010 | | 0.5279 | 0.0438 ± 0.0002 | |
| S^{100} | 0.7642 | 0.8173 ± 0.0009 | | 0.6922 | 4.2461 ± 0.0007 | | 0.3932 | 0.0704 ± 0.0027 | |
| S^{250} | 0.5136 | 3.2362 ± 0.0009 | | 0.4589 | 60.6258 ± 0.0179 | | 0.2748 | 0.1525 ± 0.0002 | |
| S^{500} | 0.4253 | 7.7012 ± 0.0038 | | 0.3278 | 706.9603 ± 0.0293 | | 0.1858 | 0.7340 ± 0.0006 | |
| S^{1000} | 0.3790 | 20.5850 ± 0.0098 | | — | — | | 0.1626 | 3.1229 ± 0.0007 | |
| E (2) | 1.9331 | 0.2723 ± 0.0013 | | 1.9330 | 0.1365 ± 0.0083 | | 1.9331 | 0.0155 ± 0.0003 | |
| E (3) | 2.0243 | 0.2852 ± 0.0017 | | 2.0233 | 0.1828 ± 0.0074 | | 2.0235 | 0.0305 ± 0.0012 | |
| E (5) | 1.8262 | 0.2996 ± 0.0079 | | 1.8047 | 0.6859 ± 0.0047 | | 1.8054 | 0.1172 ± 0.0050 | |
| E (10) | 1.5193 | 0.3094 ± 0.0086 | | 0.9472 | 57.6302 ± 0.0107 | | 1.4788 | 0.0855 ± 0.0036 | |
| E (20) | 1.2028 | 0.3379 ± 0.0049 | | 0.7603 | 48.7781 ± 0.0029 | | 1.1366 | 0.0727 ± 0.0033 | |
| E (50) | 0.8382 | 0.4596 ± 0.0092 | | 0.6157 | 153.9548 ± 0.0165 | | 0.4417 | 0.0284 ± 0.0001 | |
| E (100) | 0.6175 | 0.8219 ± 0.0036 | | 0.5822 | 3.9507 ± 0.0014 | | 0.3160 | 0.0373 ± 0.0001 | |
| E (250) | 0.4216 | 2.4940 ± 0.0028 | | 0.3882 | 48.5547 ± 0.0120 | | 0.2039 | 0.1519 ± 0.0003 | |
| E (500) | 0.3454 | 5.5967 ± 0.0145 | | — | — | | 0.1434 | 0.7326 ± 0.0005 | |
| E (1000) | 0.3056 | 14.1006 ± 0.0361 | | — | — | | 0.0996 | 4.1512 ± 0.0043 | |
| \mathbb{T}^2 | 9.8952 | 0.2821 ± 0.0029 | | 9.8943 | 38.0816 ± 0.0018 | | 9.8955 | 0.0531 ± 0.0013 | |
| \mathbb{H}^2 | 1.2435 | 0.3072 ± 0.0003 | | 1.2434 | 0.1172 ± 0.0048 | | 1.2434 | 0.0082 ± 0.0001 | |
| \mathcal{P} (2) | 1.0704 | 0.3571 ± 0.0072 | | 1.0567 | 0.1231 ± 0.0051 | | 1.0567 | 0.0243 ± 0.0002 | |
| \mathcal{P} (3) | 2.2400 | 0.3924 ± 0.0057 | | 2.3328 | 57.1278 ± 0.0125 | | 2.2304 | 0.0198 ± 0.0001 | |
| Gaussian Distribution | 2.5779 | 0.1785 ± 0.0003 | | 2.5778 | 0.0617 ± 0.0027 | | 2.5778 | 0.0130 ± 0.0002 | |
| Fréchet Distribution | 1.1471 | 0.1696 ± 0.0004 | | 1.1457 | 0.0442 ± 0.0016 | | 1.1457 | 0.0063 ± 0.0002 | |
| Cauchy Distribution | 1.6341 | 0.0230 ± 0.0002 | | 1.6340 | 0.0810 ± 0.0037 | | 1.6340 | 0.0135 ± 0.0003 | |
| Pareto Distribution | 0.8235 | 0.0357 ± 0.0003 | | 0.8235 | 0.0439 ± 0.0014 | | 0.8234 | 0.0052 ± 0.0003 | |

Table 4 The table shows the length of the estimated geodesics for different methods on a GPU. The methods have been stopped if the norm of the gradient was less than 10^{-4} or if a maximum of 1,000 iterations has been reached. When the computational time was longer than 24 hours, the value is set to —.

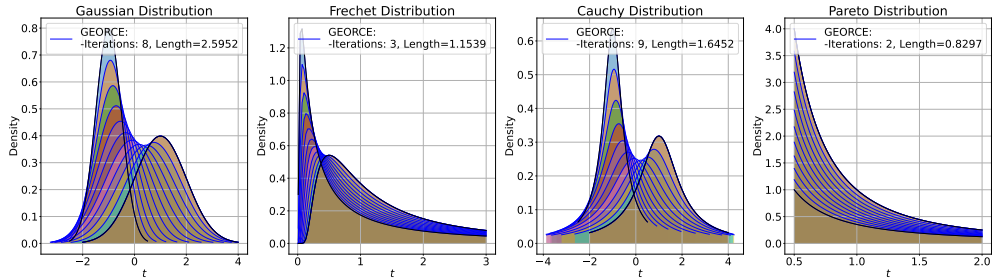


Fig. 8 The connecting geodesic between four different distributions equipped with the Fisher-Rao metric using *GEORCE*. From left to right the figures show the connecting geodesic (blue) between two fixed distributions (black) for the Gaussian distribution, Fréchet distribution, Cauchy distribution and the Pareto distribution.

the estimated geodesic between a Gaussian distribution, a Fréchet distribution, a Cauchy distribution, and a Pareto distribution using *GEORCE* all equipped with the Fisher-Rao metric in Eq. 4. The metric matrix function for the corresponding statistical manifold is described in [30]. We see that *GEORCE* converges after only a few iterations. The computed geodesics using alternative methods are summarized in Table 2, where we see that *GEORCE* obtains significantly shorter length much faster, also in high-dimension, compared to alternative methods.

We further illustrate the application of *GEORCE* to information geometry by considering potential functions encountered in Bregman geometry [18]. We consider the log-partition function for the Gaussian distribution, which is convex and smooth

$$A(\theta_1, \theta_2) = \frac{\theta_1^2}{2\theta_2} + \frac{1}{2} \log\left(\frac{2\pi}{\theta_2}\right),$$

where $\theta_1 = \frac{\mu}{\sigma^2}$ and $\theta_2 = \frac{1}{\sigma^2}$ for a Gaussian distribution with parameters (μ, σ) such that the density takes the form of an exponential family $p(x) = h(x) \exp(\theta_1 x - A(\theta_1, \theta_2))$ for a suitable h . We consider the corresponding Hessian of the log-partition function, which defines a Riemannian metric. Fig. 9 shows geodesics computed with both *GEORCE* and alternative methods that use at most 100 iterations. We see that *GEORCE* uses less iterations and obtains the smallest length compared to the alternative methods.

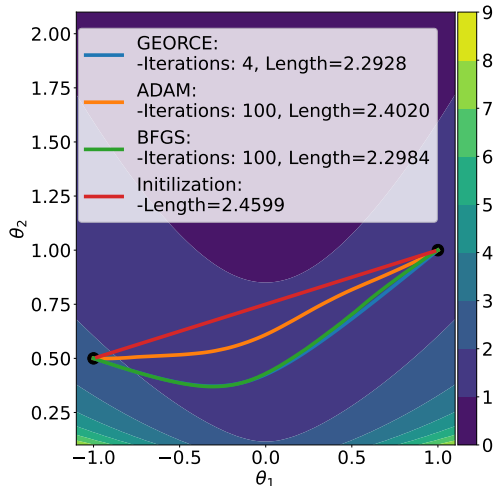


Fig. 9 The geodesics computed under the Hessian of the log-partition function of a Gaussian distribution. The background color illustrates the log-partition function.

| Finsler Manifold | BFGS ($T=100$) | | | ADAM ($T=100$) | | | GEORCE ($T=100$) | | |
|-----------------------|------------------|---------------------------|---------------|--------------------------|---------------|--|--------------------|---------|--|
| | Length | Runtime | Length | Runtime | Length | Runtime | Length | Runtime | |
| \mathbb{S}^2 | 1.6525 | 244.9129 \pm 0.0680 | 1.6536 | 0.4967 \pm 0.0007 | 1.6525 | 0.0194 \pm 0.0009 | | | |
| \mathbb{S}^3 | 1.7433 | 277.8015 \pm 0.5819 | 1.7456 | 0.7639 \pm 0.0031 | 1.7432 | 0.0362 \pm 0.0001 | | | |
| \mathbb{S}^5 | 1.7032 | 435.6987 \pm 4.6022 | 1.7377 | 4.6711 \pm 0.0047 | 1.7029 | 0.4556 \pm 0.0021 | | | |
| \mathbb{S}^{10} | 1.4151 | 812.2809 \pm 13.5968 | 1.5174 | 9.7974 \pm 0.0052 | 1.4109 | 0.7473 \pm 0.0029 | | | |
| \mathbb{S}^{20} | 1.0951 | 1446.0956 \pm 4.8038 | 1.2018 | 18.3489 \pm 0.0747 | 1.0760 | 1.2856 \pm 0.0016 | | | |
| \mathbb{S}^{50} | 0.8216 | 5992.7261 \pm 56.5973 | 0.8128 | 146.4556 \pm 0.9341 | 0.7285 | 8.4758 \pm 0.0234 | | | |
| \mathbb{S}^{100} | — | — | 0.6187 | 498.9705 \pm 0.4032 | 0.2570 | 15.3786 \pm 0.0092 | | | |
| \mathbb{S}^{250} | — | — | 0.5195 | 1397.6732 \pm 0.7793 | 0.1622 | 132.5889 \pm 0.1106 | | | |
| \mathbb{S}^{500} | — | — | 0.4850 | 1954.3231 \pm 14.1107 | 0.1404 | 364.5326 \pm 1.8222 | | | |
| \mathbb{S}^{1000} | — | — | 0.3843 | 5982.0884 \pm 204.1833 | 0.1140 | 1338.9869 \pm 2.3954 | | | |
| E (2) | 1.3616 | 230.0809 \pm 1.3967 | 1.3621 | 0.5310 \pm 0.0025 | 1.3618 | 0.0130 \pm 0.0002 | | | |
| E (3) | 1.4001 | 416.6281 \pm 5.5354 | 1.4087 | 0.8183 \pm 0.0026 | 1.4023 | 0.1081 \pm 0.0001 | | | |
| E (5) | 1.2951 | 638.7185 \pm 2.7818 | 1.3265 | 4.3802 \pm 0.0039 | 1.2956 | 0.4554 \pm 0.0014 | | | |
| E (10) | 1.0733 | 741.9274 \pm 12.3382 | 1.1229 | 9.7899 \pm 0.0117 | 1.0804 | 0.5815 \pm 0.0022 | | | |
| E (20) | 0.8510 | 1820.3137 \pm 4.0734 | 0.8980 | 19.4614 \pm 0.0039 | 0.8121 | 1.0671 \pm 0.0044 | | | |
| E (50) | 0.5981 | 11191.9424 \pm 597.7002 | 0.6325 | 146.6409 \pm 0.1668 | 0.2842 | 4.4377 \pm 0.0451 | | | |
| E (100) | — | — | 0.4936 | 491.8223 \pm 0.2346 | 0.2009 | 14.5367 \pm 0.0092 | | | |
| E (250) | — | — | 0.4159 | 1475.5049 \pm 4.1430 | 0.1287 | 125.4187 \pm 0.0888 | | | |
| E (500) | — | — | 0.4142 | 1984.7845 \pm 10.5689 | 0.0967 | 373.2816 \pm 0.4227 | | | |
| E (1000) | — | — | 0.3444 | 5929.4438 \pm 167.1873 | 0.0799 | 1211.8812 \pm 0.2511 | | | |
| \mathbb{T}^2 | 7.3890 | 449.4798 \pm 10.3282 | 7.3585 | 0.3294 \pm 0.0018 | 6.8067 | 0.1126 \pm 0.0002 | | | |
| \mathbb{H}^2 | 1.3340 | 384.3149 \pm 0.3044 | 1.3360 | 0.2744 \pm 0.0024 | 1.3337 | 0.0094 \pm 0.0001 | | | |
| \mathcal{P} (2) | 0.7291 | 414.8355 \pm 3.0837 | 0.7338 | 0.6368 \pm 0.0026 | 0.7292 | 0.0222 \pm 0.0001 | | | |
| \mathcal{P} (3) | 1.2856 | 536.6575 \pm 0.9323 | 1.2980 | 5.2824 \pm 0.0540 | 1.2856 | 0.2094 \pm 0.0004 | | | |
| Gaussian Distribution | 1.6878 | 163.4399 \pm 0.1859 | 1.6936 | 0.1145 \pm 0.0001 | 1.6878 | 0.0047 \pm 0.0001 | | | |
| Fréchet Distribution | 0.5408 | 123.8418 \pm 0.0499 | 0.5406 | 0.0585 \pm 0.0001 | 0.5405 | 0.0021 \pm 0.0001 | | | |
| Cauchy Distribution | 1.1134 | 182.3980 \pm 2.2559 | 1.1133 | 0.1105 \pm 0.0007 | 1.1133 | 0.0067 \pm 0.0002 | | | |
| Pareto Distribution | 0.3884 | 84.8186 \pm 0.0832 | 0.3885 | 0.0235 \pm 0.0007 | 0.3883 | 0.0020 \pm 0.0001 | | | |

Table 5 The length of the estimated geodesics for the *BFGS*-algorithm, *ADAM*-gradient descent and *GEORCE* on a CPU. The algorithms have been stopped if the ℓ^2 -norm of the gradient was less than 10^{-4} or if a maximum of 1,000 iterations have been reached. $E(n)$ denotes an Ellipsoid of dimension n with half axes of n equally spaced points between 0.5 and 1.0, while $\mathcal{P}(n)$ denotes the space of $n \times n$ symmetric positive definite matrices. When the computational time was longer than 24 hours, the value is set to —.

| Finsler Manifold | ADAM (T=100) | | | Sparse Newton (T=100) | | | GEORCE (T=100) | | |
|-----------------------|--------------|------------------|--|-----------------------|--------------------|--|----------------|------------------------|--|
| | Length | Runtime | | Length | Runtime | | Length | Runtime | |
| S^2 | 1.6530 | 0.7706 ± 0.0018 | | 1.6525 | 0.2512 ± 0.0089 | | 1.6525 | 0.0372 ± 0.0004 | |
| S^3 | 1.7451 | 0.7362 ± 0.0036 | | — | — | | 1.7432 | 0.0431 ± 0.0005 | |
| S^5 | 1.7371 | 0.9292 ± 0.0038 | | — | — | | 1.7029 | 0.1036 ± 0.0048 | |
| S^{10} | 1.5174 | 1.1358 ± 0.0018 | | 1.4783 | 208.1472 ± 0.0176 | | 1.4109 | 0.1000 ± 0.0033 | |
| S^{20} | 1.2009 | 1.5876 ± 0.0028 | | — | — | | 1.0760 | 0.1509 ± 0.0058 | |
| S^{50} | 0.8130 | 2.0381 ± 0.0026 | | — | — | | 0.7283 | 0.1373 ± 0.0032 | |
| S^{100} | 0.6146 | 2.7712 ± 0.0032 | | 0.6210 | 972.0195 ± 0.0307 | | 0.2553 | 0.1106 ± 0.0028 | |
| S^{250} | 0.5196 | 3.9803 ± 0.0019 | | — | — | | 0.1636 | 0.5069 ± 0.0003 | |
| S^{500} | 0.4849 | 6.6164 ± 0.0023 | | — | — | | 0.1417 | 1.6591 ± 0.0004 | |
| S^{1000} | 0.3835 | 25.4638 ± 0.1448 | | — | — | | 0.1134 | 7.9991 ± 0.0074 | |
| E (2) | 1.3634 | 0.7758 ± 0.0036 | | 1.3616 | 0.3735 ± 0.0010 | | 1.3618 | 0.0282 ± 0.0009 | |
| E (3) | 1.4085 | 0.7541 ± 0.0032 | | — | — | | 1.4023 | 0.1273 ± 0.0047 | |
| E (5) | 1.3305 | 1.0252 ± 0.0017 | | 1.5359 | 170.9661 ± 0.0296 | | 1.2956 | 0.1135 ± 0.0039 | |
| E (10) | 1.1235 | 1.1254 ± 0.0045 | | — | — | | 1.0804 | 0.0825 ± 0.0031 | |
| E (20) | 0.8987 | 1.6039 ± 0.0035 | | — | — | | 0.8121 | 0.1282 ± 0.0054 | |
| E (50) | 0.6332 | 2.0424 ± 0.0034 | | — | — | | 0.2845 | 0.0770 ± 0.0004 | |
| E (100) | 0.4953 | 2.6704 ± 0.0031 | | 0.4577 | 470.9805 ± 0.1448 | | 0.2018 | 0.1127 ± 0.0023 | |
| E (250) | 0.4179 | 4.0843 ± 0.0009 | | — | — | | 0.1287 | 0.5239 ± 0.0047 | |
| E (500) | 0.4139 | 6.9391 ± 0.0073 | | 0.2580 | 1435.3881 ± 0.0832 | | 0.0968 | 1.7109 ± 0.0010 | |
| E (1000) | 0.3442 | 25.9660 ± 0.1038 | | — | — | | 0.0798 | 7.9988 ± 0.0079 | |
| T^2 | 7.4054 | 0.8017 ± 0.0045 | | 9.1903 | 152.0036 ± 0.0158 | | 6.8067 | 0.3145 ± 0.0050 | |
| \mathbb{H}^2 | 1.3341 | 0.7949 ± 0.0072 | | 1.3338 | 0.4562 ± 0.0004 | | 1.3337 | 0.0256 ± 0.0006 | |
| \mathcal{P} (2) | 0.7334 | 0.9344 ± 0.0013 | | 0.7291 | 0.4309 ± 0.0014 | | 0.7292 | 0.0286 ± 0.0005 | |
| \mathcal{P} (3) | 1.2987 | 1.0812 ± 0.0006 | | 1.2856 | 0.6885 ± 0.0009 | | 1.2856 | 0.0365 ± 0.0005 | |
| Gaussian Distribution | 1.6879 | 0.4962 ± 0.0034 | | 1.6878 | 0.4148 ± 0.0055 | | 1.6878 | 0.0255 ± 0.0004 | |
| Fréchet Distribution | 0.5406 | 0.2307 ± 0.0069 | | 0.5405 | 0.2060 ± 0.0042 | | 0.5405 | 0.0088 ± 0.0003 | |
| Cauchy Distribution | 1.1140 | 0.4994 ± 0.0017 | | 1.1133 | 0.5167 ± 0.0042 | | 1.1133 | 0.0367 ± 0.0017 | |
| Pareto Distribution | 0.3885 | 0.1014 ± 0.0038 | | 0.3884 | 0.1042 ± 0.0031 | | 0.3883 | 0.0096 ± 0.0004 | |

Table 6 The table shows the length of the estimated geodesics for different methods on a GPU. The methods have been stopped if the norm of the gradient was less than 10^{-4} or if a maximum of 1,000 iterations has been reached. When the computational time was longer than 24 hours, the value is set to —.

| Finsler Manifold | ADAM (T=50) | | | Sparse Newton (T=50) | | | GEORCE (T=50) | | |
|-----------------------|---------------|------------------------|---------------|----------------------|---------------|------------------|---------------|------------------|--|
| | Length | Runtime | Length | Runtime | Length | Runtime | Length | Runtime | |
| S^2 | 1.6383 | 0.7833 ± 0.0056 | 1.6385 | 0.2064 ± 0.0073 | 1.6385 | 0.0457 ± 0.0004 | 1.6385 | 0.0457 ± 0.0004 | |
| S^3 | 1.7300 | 0.7587 ± 0.0049 | — | — | 1.7297 | 0.0499 ± 0.0003 | 1.7297 | 0.0499 ± 0.0003 | |
| S^5 | 1.6875 | 0.9909 ± 0.0022 | — | — | 1.6868 | 0.1432 ± 0.0050 | 1.6868 | 0.1432 ± 0.0050 | |
| S^{10} | 1.4013 | 1.1472 ± 0.0024 | — | — | 1.3908 | 0.1747 ± 0.0067 | 1.3908 | 0.1747 ± 0.0067 | |
| S^{20} | 1.0829 | 1.5583 ± 0.0016 | — | — | 1.0560 | 0.2663 ± 0.0005 | 1.0560 | 0.2663 ± 0.0005 | |
| S^{50} | 0.7427 | 1.4442 ± 0.0038 | — | — | 0.3508 | 0.0594 ± 0.0003 | 0.3508 | 0.0594 ± 0.0003 | |
| S^{100} | 0.5511 | 2.5558 ± 0.0020 | — | — | 0.2626 | 0.0850 ± 0.0024 | 0.2626 | 0.0850 ± 0.0024 | |
| S^{250} | 0.4094 | 3.8872 ± 0.0020 | — | — | 0.1686 | 0.2660 ± 0.0042 | 0.1686 | 0.2660 ± 0.0042 | |
| S^{500} | 0.3531 | 7.5214 ± 0.0022 | 0.2861 | 1388.8278 ± 0.0965 | 0.1193 | 1.1879 ± 0.0003 | 0.1193 | 1.1879 ± 0.0003 | |
| S^{1000} | 0.3269 | 13.1209 ± 0.0379 | — | — | 0.0828 | 6.0238 ± 0.0039 | 0.0828 | 6.0238 ± 0.0039 | |
| E (2) | 1.3460 | 0.1327 ± 0.0060 | 1.3460 | 0.2847 ± 0.0043 | 1.3461 | 0.0332 ± 0.0011 | 1.3461 | 0.0332 ± 0.0011 | |
| E (3) | 1.3870 | 0.7621 ± 0.0034 | — | — | 1.3826 | 0.2156 ± 0.0006 | 1.3826 | 0.2156 ± 0.0006 | |
| E (5) | 1.2780 | 0.9718 ± 0.0022 | — | — | 1.2757 | 0.1654 ± 0.0050 | 1.2757 | 0.1654 ± 0.0050 | |
| E (10) | 1.0665 | 1.1072 ± 0.0025 | — | — | 1.0126 | 0.2215 ± 0.0062 | 1.0126 | 0.2215 ± 0.0062 | |
| E (20) | 0.8405 | 1.5702 ± 0.0031 | — | — | 0.7946 | 0.1937 ± 0.0061 | 0.7946 | 0.1937 ± 0.0061 | |
| E (50) | 0.5797 | 1.4336 ± 0.0029 | — | — | — | — | — | — | |
| E (100) | 0.4334 | 2.0750 ± 0.0026 | — | — | 0.2046 | 0.0830 ± 0.0004 | 0.2046 | 0.0830 ± 0.0004 | |
| E (250) | 0.3234 | 2.8610 ± 0.0021 | — | — | 0.1365 | 0.2644 ± 0.0029 | 0.1365 | 0.2644 ± 0.0029 | |
| E (500) | 0.2862 | 5.1735 ± 0.0122 | 0.2428 | 905.0696 ± 0.0365 | 0.0940 | 0.9444 ± 0.0011 | 0.0940 | 0.9444 ± 0.0011 | |
| E (1000) | 0.2723 | 10.4951 ± 0.0347 | — | — | 0.0893 | 4.4688 ± 0.0060 | 0.0893 | 4.4688 ± 0.0060 | |
| \mathbb{H}^2 | 7.2683 | 0.7530 ± 0.0015 | 9.0475 | 78.7132 ± 0.0222 | 9.0475 | 13.7393 ± 0.0093 | 9.0475 | 13.7393 ± 0.0093 | |
| \mathcal{P} (2) | 1.3328 | 0.7454 ± 0.0052 | 1.3316 | 0.2303 ± 0.0058 | 1.3316 | 0.0317 ± 0.0003 | 1.3316 | 0.0317 ± 0.0003 | |
| \mathcal{P} (3) | 0.7249 | 0.5927 ± 0.0008 | 0.7249 | 0.2189 ± 0.0051 | 0.7249 | 0.0331 ± 0.0011 | 0.7249 | 0.0331 ± 0.0011 | |
| | 1.2710 | 1.0184 ± 0.0008 | 1.2707 | 0.4325 ± 0.0020 | 1.2707 | 0.0434 ± 0.0006 | 1.2707 | 0.0434 ± 0.0006 | |
| Gaussian Distribution | 1.6796 | 0.4337 ± 0.0111 | 1.6806 | 0.2081 ± 0.0047 | 1.6806 | 0.0282 ± 0.0017 | 1.6806 | 0.0282 ± 0.0017 | |
| Fréchet Distribution | 0.5370 | 0.0829 ± 0.0032 | 0.5370 | 0.1059 ± 0.0042 | 0.5370 | 0.0111 ± 0.0003 | 0.5370 | 0.0111 ± 0.0003 | |
| Cauchy Distribution | 1.1085 | 0.0626 ± 0.0010 | 1.1084 | 0.2270 ± 0.0081 | 1.1084 | 0.0410 ± 0.0015 | 1.1084 | 0.0410 ± 0.0015 | |
| Pareto Distribution | 0.3857 | 0.0752 ± 0.0025 | 0.3856 | 0.1054 ± 0.0028 | 0.3857 | 0.0082 ± 0.0003 | 0.3857 | 0.0082 ± 0.0003 | |

Table 7 The table shows the length of the estimated geodesics for different methods on a GPU. The methods have been stopped if the norm of the gradient was less than 10^{-4} or if a maximum of 1,000 iterations has been reached. When the computational time was longer than 24 hours, the value is set to —.

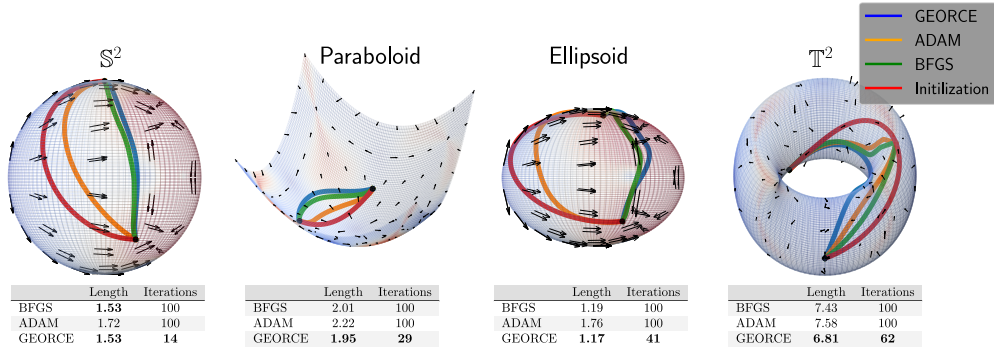


Fig. 10 Comparison between *GEORCE* and baseline methods for computing geodesics on four different Finsler manifolds. The Finsler metrics stem from a Riemannian background metric with the force field in Eq. 21 on them. The length of the force field is displayed in color, while the arrows show the direction of the force field. The algorithms are terminated if the ℓ^2 -norm of the gradient of the discretized energy functional is less than 10^{-4} , or if the number of iterations exceeds 100. We see that *GEORCE* uses less iterations and obtains the smallest length.

Finsler manifolds

To illustrate our method for different Finsler manifolds and dimensions, we consider a microswimmer on a Riemannian manifold m that moves with constant self-propulsion velocity v with Riemannian length, $v_0 := \|v\|_g$ [51] and we assume that this movement is affected by a generic force field, f , of the form

$$f(x) = \frac{\sin x \odot \cos x}{(\cos x)^\top G(x) \cos x}, \quad (21)$$

where $\cos x$ and $\sin x$ denote the element-wise function for each entry of the local coordinates x , while G denotes the corresponding Riemannian background metric such that the force field has G -length less than or equal to 1. If $\|f(x)\|_g < v_0$, then the optimal travel time of the microswimmer corresponds to a geodesic for a Finsler manifold of the form [51]

$$F = \sqrt{a_{ij} \dot{r}^i \dot{r}^j} + b_i \dot{r}^i,$$

where $a_{ij} = g_{ij} \lambda + f_i f_j \lambda^2$, $b_i = -f_i \lambda$, $b_i = -f_i \lambda$, $f_i = g_{ij} f^j$ and $\lambda^{-1} = v_0^2 - g_{ij} f^i f^j$ [51], while $r(t)$ denotes the position of the microswimmer at time t . We refer to [51] and Appendix D for details. We consider the same background metrics in Table 2 all equipped with the generic force field in Eq. 21 and compare *GEORCE* to *BFGS* [32–35] and *ADAM* [40]. Fig. 10 shows the estimated geodesics for four different Riemannian manifolds equipped with the generic force field in Eq. 21. We show the estimated geodesics for $T = 100$ grid points in Table 5. In Table 6 and Table 7 we show the corresponding results on a GPU for compatible methods for $T = 100$ and $T = 50$.

Applications to generative models

To illustrate the application of *GEORCE* to learned manifolds, we compute geodesics for generative models and compare them to similar methods. A variational autoencoder

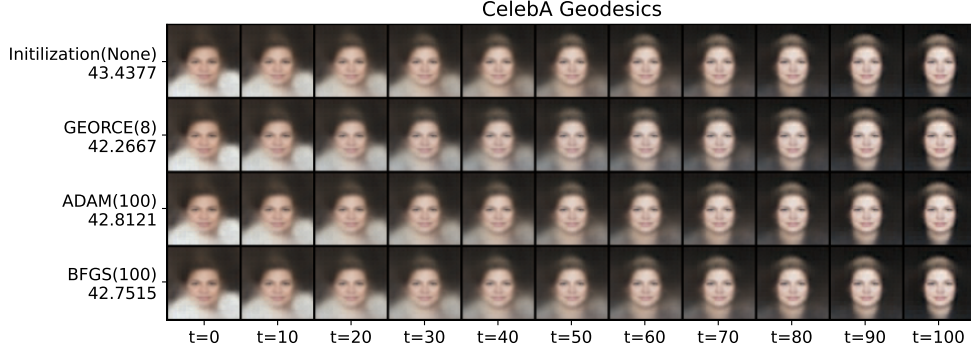


Fig. 11 Geodesics for a variational autoencoder [52] trained on the CelebA dataset [53] using *GEORCE* and alternative methods. All algorithms are terminated if the ℓ^2 -norm of the gradient of the discretized energy functional in Eq. 5 is less than 10^{-3} , or if the number of iterations exceeds 100. The algorithms are written to the left with number of iterations in parenthesis and length to the right. The first-axis shows the grid number for the image sequence. The details of the manifolds and experiments can be found Appendix E.1

(VAE) is a generative model that learns the data distribution, $\mathcal{X} \subset \mathbb{R}^D$, and a latent representation of data, $\mathcal{Z} \subset \mathbb{R}^d$, with $d < D$ by maximizing a lower bound of the log-likelihood of the data with respect to a variational family of distributions [52]

For latent space generative models, the *decoder* can be seen as a smooth d dimensional immersion, $f : \mathcal{Z} \rightarrow \mathcal{X}$, which defines a Riemannian geometry with the pull-back metric $G(z) = J_f^\top(z)J_f(z)$, where J_f denotes the Jacobian of z [11, 12].

We train a VAE for the CelebA dataset [53], which consists of 202,599 facial images of size $64 \times 64 \times 3$, where the architecture is described in Appendix E.1. Fig. 11 illustrates the geodesics constructed between two images reconstructed using the variational autoencoder. We see that *GEORCE* obtains a smaller length than comparable methods for $T = 100$ grid points. We refer to Appendix E.2 for runtime results for the VAE, where we see that *GEORCE* is significantly faster than alternative methods. Note that the tolerance for convergence is 10^{-3} , since it was observed that it was not possible for any method to obtain an ℓ^2 -norm of the gradient less than 10^{-4} . This is most likely due to potential instabilities for the learned manifold. We summarize the results in Table 8 on a CPU.

| Riemannian Manifold | BFGS (T=100) | | ADAM (T=100) | | GEORCE (T=100) | |
|---------------------|--------------|--------------------|--------------|-----------------------|----------------|---------------------------|
| | Length | Runtime | Length | Runtime | Length | Runtime |
| VAE MNIST | 10.3075 | 1407.5743 ± 6.4430 | 10.3312 | 645.5201 ± 2.6648 | 10.3074 | 67.6149 ± 0.0304 |
| VAE SVHN | — | — | 19.9855 | 13325.2285 ± 123.4978 | 19.9346 | 882.4120 ± 1.8839 |
| VAE CelebA | — | — | — | — | 42.2666 | 2222.5259 ± 8.2988 |

Table 8 The table shows the length of the estimated geodesics for the *BFGS*-algorithm, *ADAM* and *GEORCE* on a CPU. The methods were terminated if the ℓ^2 -norm of the gradient was less than 10^{-3} or 1,000 iterations have been reached. When the computational time was longer than 24 hour, the value is set to —.

6 Conclusion

In this paper, we have introduced the algorithm *GEORCE* for estimating geodesics between any given points on Riemannian and Finsler manifolds by formulating the discretized energy functional as a control problem. We have proved that *GEORCE* has global convergence and quadratic local convergence, and thus, *GEORCE* exhibits similar global convergence as gradient descent as well as local quadratic convergence similar to the Newton method without using second order derivatives. *GEORCE* scales cubically in the manifold dimension and only linearly in the number of grid points. Empirically, we have shown that *GEORCE* exhibits superior convergence in terms of runtime and accuracy compared to other geodesic optimization algorithms for Riemannian and Finsler manifolds across both dimensions and manifolds.

Limitations: *GEORCE* exhibits both global convergence and local quadratic convergence requiring few iterations. However, *GEORCE* requires evaluating the inverse matrix of the metric matrix function in each iteration, which can be numerically expensive. In addition, *GEORCE* uses line search to determine the step size in each iteration, and if it is numerically expensive to evaluate the discretized energy functional, then this can potentially increase the runtime of *GEORCE*. Further research should therefore investigate efficient approximations of the inverse metric matrix function as well as possible adaptive updating schemes for the step size to increase computational efficiency for high-dimensional problems.

Supplementary information. The supplementary information in the paper consists of the appendix for proofs, details on experiments and manifolds as well as additional experiments.

Acknowledgements. Many thanks to Prof. Steen Markvorsen and Dr. Andreas A. Bock for comments and corrections in the process of writing this paper. Especially, a thanks to Prof. Steen Markvorsen for hinting at the possible extension to Finsler geometry. SH is supported by a research grant (42062) from VILLUM FONDEN. This project received funding from the European Research Council (ERC) under the European Union’s Horizon research and innovation programme (grant agreement 101125993). The work was partly funded by the Novo Nordisk Foundation through the Center for Basic Machine Learning Research in Life Science (NNF20OC0062606).

Declarations

- Funding: Research grant 42062 from VILLUM FONDEN; funding from the European Research Council (ERC) under the European Union’s Horizon research and innovation programme (grant agreement 101125993); funding from the Novo Nordisk Foundation through the Center for Basic Machine Learning Research in Life Science (NNF20OC0062606).
- Conflict of interest/Competing interests: NA
- Ethics approval and consent to participate: NA
- Consent for publication: Currently under review.
- Data availability: All data used are described in the appendix.
- Materials availability: NA

- Code availability: The code can be found at <https://github.com/FrederikMR/georce>
- Author contribution: FMR derived the algorithm and implemented the method as well as benchmarks. SH supervised the project with comments and corrections. The paper was written jointly by SH and FMR. All authors reviewed the manuscript.

References

- [1] Pennec, X., Sommer, S. & Fletcher, T. *Riemannian Geometric Statistics in Medical Image Analysis* (Academic Press, 2019).
- [2] Pennec, X., Ayache, N. & Thirion, J.-P. *Landmark-based registration using features identified through differential geometry*, 499–513 (Academic Press, Inc., USA, 2000).
- [3] Lenglet, C., Rousson, M., Deriche, R. & Faugeras, O. Statistics on Multivariate Normal Distributions: A Geometric Approach and its Application to Diffusion Tensor MRI. *Rapport de recherche, Institut National de Recherche en Informatique et en Automatique (INRIA)* (2004).
- [4] Watson, Z., Townshend, R. J. L. & Dror, R. O. Protein Design Using Diffusion Models. *bioRxiv* (2022). URL <https://www.biorxiv.org/content/10.1101/2022.12.09.519842v1>.
- [5] Deftelsen, N. & Others. Protein Structure Prediction Using Rosetta. *Methods in Molecular Biology* **2021**, 1–30 (2019).
- [6] Shapovalov, M. & Dunbrack, R. A Smoothed Backbone-Dependent Rotamer Library for Proteins Derived from Adaptive Kernel Density Estimates and Regressions. *Structure (London, England : 1993)* **19**, 844–58 (2011).
- [7] Hsieh, M. A. *et al.* Reactive Motion Generation on Learned Riemannian Manifolds. *Int. J. Rob. Res.* **42**, 729–754 (2023). URL <https://doi.org/10.1177/02783649231193046>.
- [8] Simeonov, A. *et al.* Neural Descriptor Fields: SE(3)-Equivariant Object Representations for Manipulation (2022).
- [9] Senanayake, R. & Ramos, F. T. Directional Grid Maps: Modeling Multimodal Angular Uncertainty in Dynamic Environments. *2018 IEEE/RSJ International Conference on Intelligent Robots and Systems (IROS)* 3241–3248 (2018). URL <https://api.semanticscholar.org/CorpusID:52158241>.
- [10] Feiten, W., Lang, M. & Hirche, S. Rigid Motion Estimation Using Mixtures of Projected Gaussians 1465–1472 (2013).
- [11] Arvanitidis, G., Hansen, L. K. & Hauberg, S. Latent Space Oddity: on the Curvature of Deep Generative Models (2018). URL <https://openreview.net/forum?id=SJzRZ-WCZ>.
- [12] Shao, H., Kumar, A. & Thomas Fletcher, P. The Riemannian Geometry of Deep Generative Models (2018).

- [13] Bortoli, V. D. *et al.* Oh, A. H., Agarwal, A., Belgrave, D. & Cho, K. (eds) *Riemannian Score-Based Generative Modelling*. (eds Oh, A. H., Agarwal, A., Belgrave, D. & Cho, K.) *Advances in Neural Information Processing Systems* (2022). URL <https://openreview.net/forum?id=oDRQGo8I7P>.
- [14] Jo, J. & Hwang, S. J. Generative Modeling on Manifolds through Mixture of Riemannian Diffusion Processes (2024).
- [15] Mathieu, E. & Nickel, M. Riemannian Continuous Normalizing Flows (2020).
- [16] Rozen, N., Grover, A., Nickel, M. & Lipman, Y. Moser Flow: Divergence-based Generative Modeling on Manifolds (2021).
- [17] Arvanitidis, G., González-Duque, M., Pouplin, A., Kalatzis, D. & Hauberg, S. Camps-Valls, G., Ruiz, F. J. R. & Valera, I. (eds) *Pulling back information geometry*. (eds Camps-Valls, G., Ruiz, F. J. R. & Valera, I.) *Proceedings of The 25th International Conference on Artificial Intelligence and Statistics*, Vol. 151 of *Proceedings of Machine Learning Research*, 4872–4894 (PMLR, 2022). URL <https://proceedings.mlr.press/v151/arvanitidis22b.html>.
- [18] Nielsen, F. An Elementary Introduction to Information Geometry. *Entropy* **22**, 1100 (2020). URL <http://dx.doi.org/10.3390/e22101100>.
- [19] Cheng, C., Li, J., Peng, J. & Liu, G. Globerson, A. *et al.* (eds) *Categorical Flow Matching on Statistical Manifolds*. (eds Globerson, A. *et al.*) *Advances in Neural Information Processing Systems*, Vol. 37, 54787–54819 (Curran Associates, Inc., 2024). URL https://proceedings.neurips.cc/paper_files/paper/2024/file/62a58f2130894e44e8a272c563a2c6f1-Paper-Conference.pdf.
- [20] Myers, V., Ellis, E., Levine, S., Eysenbach, B. & Dragan, A. Learning to Assist Humans without Inferring Rewards (2024). URL <https://openreview.net/forum?id=WCnJmb7cv1>.
- [21] Davis, O. *et al.* Globerson, A. *et al.* (eds) *Fisher Flow Matching for Generative Modeling over Discrete Data*. (eds Globerson, A. *et al.*) *Advances in Neural Information Processing Systems*, Vol. 37, 139054–139084 (Curran Associates, Inc., 2024). URL https://proceedings.neurips.cc/paper_files/paper/2024/file/fadec8f2e65f181d777507d1df69b92f-Paper-Conference.pdf.
- [22] Hauberg, S. *Differential Geometry for Generative Modeling* (2025).
- [23] do Carmo, M. *Riemannian Geometry* Mathematics (Boston, Mass.) (Birkhäuser, 1992). URL <https://books.google.dk/books?id=uXJQQgAACAAJ>.
- [24] Detlefsen, N. S. *et al.* StochMan. *GitHub*. Note: <https://github.com/MachineLearningLifeScience/stochman/> (2021).

- [25] Noakes, L. A Global algorithm for geodesics. *Journal of the Australian Mathematical Society. Series A. Pure Mathematics and Statistics* **65**, 37–50 (1998).
- [26] Tosi, A., Hauberg, S., Vellido, A. & Lawrence, N. D. Metrics for probabilistic geometries (2014).
- [27] Nash, J. C1 Isometric Imbeddings. *Annals of Mathematics* **60**, 383–396 (1954). URL <http://www.jstor.org/stable/1969840>.
- [28] Whitney, H. Differentiable Manifolds. *Annals of Mathematics* **37**, 645–680 (1936). URL <http://www.jstor.org/stable/1968482>.
- [29] Ohta, S. *Comparison Finsler Geometry* Springer Monographs in Mathematics (Springer International Publishing, 2021). URL <https://books.google.dk/books?id=4Mh6zgEACAAJ>.
- [30] Miyamoto, H. K., Meneghetti, F. C. C., Pinele, J. & Costa, S. I. R. On Closed-Form Expressions for the Fisher-Rao Distance. *Information Geometry* **7** (2024).
- [31] Peter, A. & Rangarajan, A. Shape analysis using the Fisher-Rao Riemannian metric: Unifying shape representation and deformation. In: *IEEE ISBI. IEEE* **2006**, 1164–1167 (2006).
- [32] Broyden, C. G. The Convergence of a Class of Double-rank Minimization Algorithms 1. General Considerations. *IMA Journal of Applied Mathematics* **6**, 76–90 (1970). URL <https://doi.org/10.1093/imamat/6.1.76>.
- [33] Fletcher, R. A new approach to variable metric algorithms. *The Computer Journal* **13**, 317–322 (1970). URL <https://doi.org/10.1093/comjnl/13.3.317>.
- [34] A family of variable-metric methods derived by variational means, author=Donald Goldfarb. *Mathematics of Computation* **24**, 23–26 (1970). URL <https://api.semanticscholar.org/CorpusID:790344>.
- [35] Shanno, D. & Kettler, P. Optimal Conditioning of Quasi-Newton Methods. *Mathematics of Computation - Math. Comput.* **24**, 657–657 (1970).
- [36] Luenberger, D. & Ye, Y. *Linear and Nonlinear Programming* International Series in Operations Research & Management Science (Springer US, 2008). URL <https://books.google.dk/books?id=-pD62uvi9lgC>.
- [37] Kaya, C. Y. & Noakes, J. L. Leapfrog for Optimal Control. *SIAM Journal on Numerical Analysis* **46**, 2795–2817 (2008). URL <https://doi.org/10.1137/060675034>.
- [38] Hennig, P. & Hauberg, S. Kaski, S. & Corander, J. (eds) *Probabilistic Solutions to Differential Equations and their Application to Riemannian Statistics*. (eds Kaski,

- S. & Corander, J.) *Proceedings of the Seventeenth International Conference on Artificial Intelligence and Statistics*, Vol. 33 of *Proceedings of Machine Learning Research*, 347–355 (PMLR, Reykjavik, Iceland, 2014). URL <https://proceedings.mlr.press/v33/hennig14.html>.
- [39] Arvanitidis, G., Hauberg, S., Hennig, P. & Schober, M. Chaudhuri, K. & Sugiyama, M. (eds) *Fast and Robust Shortest Paths on Manifolds Learned from Data*. (eds Chaudhuri, K. & Sugiyama, M.) *Proceedings of the Twenty-Second International Conference on Artificial Intelligence and Statistics*, Vol. 89 of *Proceedings of Machine Learning Research*, 1506–1515 (PMLR, 2019). URL <https://proceedings.mlr.press/v89/arvanitidis19a.html>.
- [40] Kingma, D. P. & Ba, J. Adam: A Method for Stochastic Optimization (2014). URL <http://arxiv.org/abs/1412.6980>. Cite arxiv:1412.6980Comment: Published as a conference paper at the 3rd International Conference for Learning Representations, San Diego, 2015.
- [41] Crane, K., Livesu, M., Puppo, E. & Qin, Y. A Survey of Algorithms for Geodesic Paths and Distances. *CoRR* **abs/2007.10430** (2020). URL <https://arxiv.org/abs/2007.10430>.
- [42] Surazhsky, V., Surazhsky, T., Kirsanov, D., Gortler, S. J. & Hoppe, H. Fast exact and approximate geodesics on meshes. *ACM Trans. Graph.* **24**, 553–560 (2005). URL <https://doi.org/10.1145/1073204.1073228>.
- [43] Chen, J. & Han, Y. Shortest paths on a polyhedron. *Proceedings of the Sixth Annual Symposium on Computational Geometry* 360–369 (1990). URL <https://doi.org/10.1145/98524.98601>.
- [44] Xin, S.-Q. & Wang, G.-J. Improving Chen and Han’s Algorithm on the Discrete Geodesic Problem. *ACM Trans. Graph.* **28** (2009).
- [45] Qin, Y., Han, X., Yu, H., Yu, Y. & Zhang, J. Fast and exact discrete geodesic computation based on triangle-oriented wavefront propagation. *ACM Trans. Graph.* **35** (2016). URL <https://doi.org/10.1145/2897824.2925930>.
- [46] Beik-Mohammadi, H., Hauberg, S., Arvanitidis, G., Neumann, G. & Rozo, L. Learning Riemannian Manifolds for Geodesic Motion Skills (2021).
- [47] Kirk, D. *Optimal Control Theory: An Introduction* Dover Books on Electrical Engineering Series (Dover Publications, 2004). URL <https://books.google.dk/books?id=fCh2SAtWIdwC>.
- [48] Boyd, S. P. & Vandenberghe, L. *Convex Optimization* (Cambridge University Press, Cambridge, UK, 2004).

- [49] Wolfe, P. Convergence Conditions for Ascent Methods. *SIAM Review* **11**, 226–235 (1969). URL <https://doi.org/10.1137/1011036>.
- [50] Armijo, L. Minimization of functions having Lipschitz continuous first partial derivatives. *Pacific Journal of Mathematics* **16**, 1–3 (1966).
- [51] Piro, L., Tang, E. & Golestanian, R. Optimal navigation strategies for microswimmers on curved manifolds. *Physical Review Research* **3** (2021). URL <http://dx.doi.org/10.1103/PhysRevResearch.3.023125>.
- [52] Kingma, D. P. & Welling, M. Auto-Encoding Variational Bayes (2014). <http://arxiv.org/abs/1312.6114v10>.
- [53] Liu, Z., Luo, P., Wang, X. & Tang, X. Deep Learning Face Attributes in the Wild. *Proceedings of International Conference on Computer Vision (ICCV)* (2015).
- [54] Thomas, L. Elliptic Problems in Linear Difference Equations over a Network (1949).
- [55] Noakes, L. & Zhang, E. Finding geodesics joining given points. *Advances in Computational Mathematics* **48** (2022).
- [56] Deng, L. The mnist database of handwritten digit images for machine learning research. *IEEE Signal Processing Magazine* **29**, 141–142 (2012).
- [57] Netzer, Y. *et al.* Reading Digits in Natural Images with Unsupervised Feature Learning. *NIPS Workshop on Deep Learning and Unsupervised Feature Learning 2011* (2011). URL http://ufdl.stanford.edu/housenumbers/nips2011_housenumbers.pdf.
- [58] Ruder, S. An Overview of Gradient Descent Optimization Algorithms (2017). URL <https://arxiv.org/abs/1609.04747>. arXiv:1609.04747.
- [59] Nocedal, J. & Wright, S. *Numerical Optimization* Springer Series in Operations Research and Financial Engineering (Springer New York, 2006). URL <https://books.google.dk/books?id=VbHYoSyeIFcC>.
- [60] Virtanen, P. *et al.* SciPy 1.0: Fundamental Algorithms for Scientific Computing in Python. *Nature Methods* **17**, 261–272 (2020).
- [61] Dormand, J. & Prince, P. A Family of Embedded Runge-Kutta Formulae. *Journal of Computational and Applied Mathematics* **6**, 19–26 (1980). URL <https://www.sciencedirect.com/science/article/pii/0771050X80900133>.
- [62] Bogacki, P. & Shampine, L. A 3(2) Pair of Runge - Kutta Formulas. *Applied Mathematics Letters* **2**, 321–325 (1989). URL <https://www.sciencedirect.com/science/article/pii/0893965989900797>.

- [63] Hairer, E., Norsett, S. & Wanner, G. *Solving Ordinary Differential Equations I: Nonstiff Problems* Vol. 8 (1993).
- [64] Hairer, E. & Wanner, G. *Solving Ordinary Differential Equations II. Stiff and Differential-Algebraic Problems* Vol. 14 (1996).
- [65] Shampine, L. F. & Reichelt, M. W. The MATLAB ODE Suite. *SIAM Journal on Scientific Computing* **18**, 1–22 (1997). URL <https://doi.org/10.1137/S1064827594276424>.
- [66] Hindmarsh, A. C. Stepleman, R. S. (ed.) *ODEPACK, a Systematized Collection of ODE Solvers*. (ed. Stepleman, R. S.) *Scientific Computing*, 55–64 (North-Holland, Amsterdam, 1983).

Appendix A Proofs and derivations

A.1 Proof of update scheme for Finslerian geometry

Consider the following control problem in the Finslerian case.

$$\begin{aligned}
\min_{x_0:T} \quad & \sum_{t=0}^{T-1} u_t^\top G(x_t, u_t) u_t, \quad t = 0, \dots, T-1, \\
\text{s.t.} \quad & x_{t+1} = x_t + u_t \\
& x_0 = a, x_T = b,
\end{aligned} \tag{A1}$$

By similar computation as in Proposition. 1 with G is now dependent on both x_t and u_t , we get the following equation system to be solved in iteration $i + 1$ derived from Pontryagin's maximum principle by fixing variables

$$\begin{aligned}
\nu_t + \mu_t &= \mu_{t-1}, \quad t = 1, \dots, T-1, \\
2G_t u_t + \zeta_t + \mu_t &= 0, \quad t = 0, \dots, T-1, \\
\sum_{t=0}^{T-1} u_t &= b - a, \\
\nu_t &:= \nabla_y (u_t^\top G(y, u_t) u_t) \Big|_{y=x_t^{(i)}, u_t=u_t^{(i)}}, \quad t = 1, \dots, T-1, \\
\zeta_t &:= \nabla_y (u_t^\top G(x_t, y) u_t) \Big|_{x_t=x_t^{(i)}, u_t=u_t^{(i)}, y=u_t^{(i)}}, \quad t = 1, \dots, T-1, \\
G_t &:= G(x_t^{(i)}, u_t^{(i)}), \quad t = 0, \dots, T-1,
\end{aligned} \tag{A2}$$

The related state variables (before line search) are found by the state equation, $x_{t+1} = x_t + u_t$ for $t = 0, \dots, T-1$ with $x_0 = a$. Using the same approach as in the proof of Proposition 2, then Eq. A2 is equivalent to

$$\begin{aligned}
\mu_{T-1} &= \left(\sum_{t=0}^{T-1} G_t^{-1} \right)^{-1} \left(2(a-b) - \sum_{t=0}^{T-1} G_t^{-1} \left(\zeta_t + \sum_{t>j}^{T-1} \nu_j \right) \right), \\
u_t &= -\frac{1}{2} G_t^{-1} \left(\mu_{T-1} + \zeta_t + \sum_{j>t}^{T-1} \nu_j \right), \quad t = 0, \dots, T-1, \\
x_{t+1} &= x_t + u_t, \quad t = 0, \dots, T-1, \\
x_0 &= a,
\end{aligned} \tag{A3}$$

where it is exploited that the fundamental tensor is positive definite.

A.2 Extension to Finslerian manifolds

The proof for global convergence and local quadratic convergence hold similar for *GEORCE* in the Finsler case. Let E_F denote the corresponding discretized Finsler

energy functional. For the Finsler case the optimally condition becomes

$$\begin{aligned}\nabla_{x_t} E_F(x_t, u_{t0}) \Big|_{(x_t, u_t) = (x_t^{(i)}, u_t^{(i)})} &= \mu_{T-1} - \mu_t, \quad t = 1, \dots, T-1, \\ \nabla_{u_t} E_F(x_t, u_t) \Big|_{(x_t, u_t) = (x_t^{(i)}, u_t^{(i+1)})} &= 2G(x_t^{(i)}, u_t^{(i)}) u_t^{(i+1)} + \zeta_t = -\mu_t, \\ &t = 0, \dots, T-1\end{aligned}\tag{A4}$$

The proof of global and local quadratic convergence is completely similar for the Riemannian and Finsler case except that Eq. 14 in the Finsler case becomes

$$\begin{aligned}\mu_t + \nabla_{u_t} E_F(x_t, u_t) \Big|_{(x_t, u_t) = (x_t^{(i)}, u_t^{(i)})} &= -\nabla_{u_t} E_F(x_t, u_t) \Big|_{(x_t, u_t) = (x_t^{(i+1)}, u_t^{(i+1)})} \\ &+ \nabla_{u_t} E_F(x_t, u_t) \Big|_{(x_t, u_t) = (x_t^{(i+1)}, u_t^{(i)})} \\ &= -\left(G(x_t^{(i)}, u_t^{(i)}) u_t^{(i+1)} + \zeta_t\right) \\ &+ \left(2G(x_t^{(i)}, u_t^{(i)}) + \zeta_t\right) \\ &= -2G(x_t^{(i)}, u_t^{(i)}) \left(u_t^{(i+1)} - u_t^{(i)}\right),\end{aligned}\tag{A5}$$

by using the properties of *GEORCE* in the Finsler case in Eq. A4. Eq. A5 is completely similar to Eq. 14 in the Riemannian case, and from that the global convergence and local quadratic convergence proofs are completely similar to the Riemannian case.

Appendix B Algorithms

B.1 GEORCE for Finsler manifolds

In Algorithm 2 we show *GEORCE* for Finsler manifolds in pseudo-code using the update scheme in Eq. 20.

B.2 Sparse Newton Method

In this section we derive a sparse Newton method for minimizing Eq. 5. We consider the Riemannian case, but note that it is easily generalized to the Finslerian case. The Hessian of the Eq. 5 we get that

$$\begin{aligned}\partial_{x_t x_t}^2 E(x_{0:T}) &= \partial_{x_t x_t}^2 u_t^\top G(x_t) u_t \Big|_{u_t = x_{t+1} - x_t} + 2G(x_{t-1}) - 2G(x_t) \\ &+ 4\nabla_{x_{t-1}} G(x_{t-1}) u_t \Big|_{u_t = x_t - x_{t-1}} - 4\nabla_{x_t} G(x_t) u_t \Big|_{u_t = x_{t+1} - x_t}, \quad t = 1, \dots, T-1, \\ \partial_{x_t x_{t+1}}^2 E(x_{0:T}) &= 2\nabla_{x_t} G(x_t) u_t \Big|_{u_t = x_{t+1} - x_t}, \quad t = 1, \dots, T-2, \\ \partial_{x_{t+1} x_t}^2 E(x_{0:T}) &= 2(G(x_t) u_t)^\top \Big|_{u_t = x_{t+1} - x_t}, \quad t = 1, \dots, T-2.\end{aligned}$$

Algorithm 2 GEORCE for Finsler Manifolds

- 1: **Input:** tol, T
 - 2: **Output:** Geodesic estimate $x_{0:T}$
 - 3: Set $x_t^{(0)} \leftarrow a + \frac{b-a}{T}t$, $u_t^{(0)} \leftarrow \frac{b-a}{T}$ for $t = 0, \dots, T$ and $i \leftarrow 0$
 - 4: **while** $\left\| \nabla_y E(y) \Big|_{y=x_t^{(i)}} \right\|_2 > \text{tol}$ **do**
 - 5: $G_t \leftarrow G(x_t^{(i)}, u_t^{(i)})$ for $t = 0, \dots, T-1$
 - 6: $\nu_t \leftarrow \nabla_y (u_t^{(i)} G(y, u_t^{(i)})) \Big|_{y=x_t^{(i)}}$ for $t = 1, \dots, T-1$
 - 7: $\zeta_t \leftarrow \nabla_y (u_t^{(i)} G(x_t^{(i)}, y)) \Big|_{y=u_t^{(i)}}$ for $t = 1, \dots, T-1$
 - 8: $\mu_{T-1} \leftarrow \left(\sum_{t=0}^{T-1} G_t^{-1} \right)^{-1} \left(2(a-b) - \sum_{t=0}^{T-1} G_t^{-1} \left(\zeta_t + \sum_{t>j}^{T-1} \nu_j \right) \right)$
 - 9: $u_t \leftarrow -\frac{1}{2} G_t^{-1} \left(\mu_{T-1} + \zeta_t + \sum_{j>t}^{T-1} \nu_j \right)$ for $t = 0, \dots, T-1$
 - 10: $x_{t+1} \leftarrow x_t + u_t$ for $t = 0, \dots, T-1$
 - 11: Using line search find α^* for the following optimization problem with the discrete energy functional E_F

$$\alpha^* = \arg \min_{\alpha} E_F(x_{0:T}) \quad (\text{exact line-search})$$

$$\text{s.t. } x_{t+1} = x_t + \alpha u_t + (1-\alpha)u_t^{(i)}, \quad t = 0, \dots, T-1,$$

$$x_0 = a.$$
 - 12: Set $u_t^{(i+1)} \leftarrow \alpha^* u_t + (1-\alpha^*)u_t^{(i)}$ for $t = 0, \dots, T-1$
 - 13: Set $x_{t+1}^{(i+1)} \leftarrow x_t^{(i+1)} + u_t^{(i+1)}$ for $t = 0, \dots, T-1$
 - 14: $i \leftarrow i+1$
 - 15: **end while**
 - 16: return x_t for $t = 0, \dots, T-1$
-

where ∂_{x_i, x_j}^2 denotes the second order derivative. From this we see that the Hessian can be written as

$$H = \begin{pmatrix} H_{11} & H_{12} & 0 & 0 & 0 & 0 & 0 & \dots & 0 \\ H_{21} & H_{22} & H_{23} & 0 & 0 & 0 & 0 & \dots & 0 \\ 0 & H_{23} & H_{33} & H_{34} & 0 & 0 & 0 & \dots & 0 \\ 0 & 0 & H_{43} & H_{33} & H_{45} & 0 & 0 & \dots & 0 \\ 0 & 0 & 0 & H_{54} & H_{55} & H_{56} & 0 & \dots & 0 \\ 0 & 0 & 0 & 0 & H_{65} & H_{66} & H_{67} & \dots & 0 \\ \vdots & \ddots & \vdots \\ 0 & 0 & 0 & 0 & 0 & 0 & \dots & H_{(T-2)(T-2)} & H_{(T-1)(T-2)} \\ 0 & 0 & 0 & 0 & 0 & 0 & \dots & H_{(T-2)(T-1)} & H_{(T-1)(T-1)} \end{pmatrix}, \quad (\text{B6})$$

where we define

$$H_{ij} = \partial_{x_i x_j}^2 E(x_{0:T}),$$

A Newton step has the following form at iteration j .

$$s^{(j)} = -H^{-1} \nabla_{x_{1:(T-1)}} E(x_{0:T}), \quad (\text{B7})$$

To simplify notation, define $s_i := -\nabla_{x_i} E(x_{0:T})$. Using the block structure in Eq. B6, we can recursively solve Eq. B7 similar to the Thomas Algorithm [54].

$$\begin{aligned} s_i &\leftarrow H_{ii}^{-1} s_i, \\ P &\leftarrow H_{ii+1}^\top, \quad i+1 < T \\ H_{ii+1} &\leftarrow H_{ii}^{-1} H_{ii+1}, \quad i+1 < T \\ H_{i+1,i+1} &\leftarrow H_{i+1,i+1} - H_{i+1,i} H_{i,i+1} = H_{i+1,i+1} - P H_{i,i+1}, \quad i+1 < T \\ s_{i+1} &\leftarrow s_{i+1} - H_{i+1,i} s_i = s_{i+1} - P s_i, \quad i+1 < T. \end{aligned} \quad (\text{B8})$$

such that the Newton step is updated for $i = T-2, \dots, 1$

$$s_i \leftarrow s_i - H_{i,i+1} s_{i+1}. \quad (\text{B9})$$

Note that we efficiently solve the equations in Eq. B8 as

$$\begin{aligned} H_{ii} y_i &= (H_{ii+1} | s_i), \quad i = 1, \dots, T-2, \\ H_{T-1} y_{T-1} &= s_{T-1}, \end{aligned} \quad (\text{B10})$$

such that only one linear system of equations has to be solved in each iteration. The Newton method does not have global convergence. In Algorithm 3 we write the Sparse Newton algorithm in pseudo-code switching between the Newton method and gradient descent with line-search. Note that the above is easily extended to the Finslerian case, where G denotes the fundamental tensor and depends on both x and u . Note that the sparse Newton algorithm in Algorithm 3 has complexity $\mathcal{O}(Td^3)$ completely similar to GEORCE.

Since the Hessian of the energy is not necessarily positive definite, the Newton scheme can be numerically unstable. To avoid this, we represent in Algorithm 4 a regularized Newton method by adding suitable scaling in the diagonal. Note that the Newton method for the discretized energy was also proposed in [55], which also formulates the Hessian as a block matrix similar to Eq. B6. However, they do not derive an adaptive scheme to solve the linear equation in the Newton step or propose the regularized version in Algorithm 4.

Algorithm 3 Sparse Newton Method

1: **Input:** tol, T
2: **Output:** Geodesic estimate $x_{0:T}$
3: Set $x_t^{(0)} \leftarrow a + \frac{b-a}{T}t$ for $t = 0, \dots, T$ and $j \leftarrow 0$
4: **while** $\left\| \nabla_y E(y) \Big|_{y=x_t^{(j)}} \right\|_2 > \text{tol}$ **do**
5: Compute $\left\{ s_t^{\text{grad}}, s_t^{\text{newton}} \right\}_{t=1, \dots, T-2}$ using Eq. B8 and Eq. B9.
6: **if then** $\sum_{t=1}^{T-1} s_t^{\text{grad}} (s_t^{\text{newton}})^\top \geq 0$
7: $s_t = s_t^{\text{newton}}$ for $t = 1, \dots, T-1$
8:
9: **else**
10: $s_t = s_t^{\text{grad}}$ for $t = 1, \dots, T-1$
11: **end if**
12: Perform line-search for $\alpha^* = \arg \min_{0 \leq \alpha \leq 1} E(x_{1:(T-1)} + \alpha s_{1:(T-1)})$ with
$$x_t^{(j+1)} \leftarrow x_t^{(j)} + \alpha^* s_t, \quad t = 1, \dots, T-1.$$

13: $j \leftarrow j + 1$
14: **end while**
15: return $x_t^{(j)}$ for $t = 0, \dots, T-1$

Algorithm 4 Sparse Regularized Newton Method

```
1: Input: tol,  $T$ ,  $\lambda$ ,  $\kappa$ 
2:
3: Output: Geodesic estimate  $x_{0:T}$ 
4:
5: Set  $x_t^{(0)} \leftarrow a + \frac{b-a}{T}t$  for  $t = 0, \dots, T$  and  $j \leftarrow 0$ 
6:
7: while  $\left\| \nabla_y E(y) \Big|_{y=x_t^{(j)}} \right\|_2 > \text{tol}$  do
8:    $H_{ii} \leftarrow \lambda I + \partial_{x_i x_i}^2 E(x_{0:T})$ 
9:
10:   $H_{ij} \leftarrow \partial_{x_i x_j}^2 E(x_{0:T})$ 
11:
12:  Compute  $\left\{ s_t^{\text{grad}}, s_t^{\text{newton}} \right\}_{t=1, \dots, T-2}$  using Eq. B8 and Eq. B9.
13:
14:  if then  $\sum_{t=1}^{T-1} s_t^{\text{grad}} (s_t^{\text{newton}})^\top \geq 0$ 
15:
16:     $s_t = s_t^{\text{newton}}$  for  $t = 1, \dots, T-1$ 
17:
18:     $\lambda \leftarrow \kappa \lambda$ 
19:  else
20:     $s_t = s_t^{\text{grad}}$  for  $t = 1, \dots, T-1$ 
21:
22:     $\lambda \leftarrow \lambda / \kappa$ 
23:  end if
24:  Perform line-search for  $\alpha^* = \arg \min_{0 \leq \alpha \leq 1} E(x_{1:(T-1)} + \alpha s_{1:(T-1)})$  with
      
$$x_t^{(j+1)} \leftarrow x_t^{(j)} + \alpha^* s_t, \quad t = 1, \dots, T-1.$$

25:   $j \leftarrow j + 1$ 
26: end while
27: return  $x_t^{(j)}$  for  $t = 0, \dots, T-1$ 
```

Appendix C Choice of initialization curve

In this section, we show the effect of the choice of initialization curve in *GEORCE*. In Algorithm 1 and the experiments, the initial curve is a straight line between the start and end point. However, the initial curve is not restricted to this and can in principle be any curve assuming that it is defined in the local chart. To illustrate the effect of the initial curve, we will consider the egg-tray with the parametrization $f(x, y) = (x, y, 2 \cos x \cos y)$, and the sphere for two antipodal points on the equator. For the egg-tray we consider setting the initial curve randomly as

$$x_t^{(0)} = t \frac{b-a}{T} + a + \epsilon_t, \quad \epsilon_t \sim \mathcal{N}(0, I),$$

while we consider for the sphere the random initial curve.

$$x_t^{(0)} = t \frac{b-a}{T} + a + \mathbf{1} \text{Sign}(\epsilon), \quad \epsilon \sim \mathcal{N}(0, 1),$$

For each random initial curve, we estimate the energy-minimizing curve using *GEORCE* and show the result in Fig. C1 for 100 random initializations. The first row shows the results for the egg-tray, where the rightmost figure is the distribution of length for the computed curves. We display the corresponding curves in the same color as in the histogram. In general, we see that for a small set of curves *GEORCE* has found a local minimum, where the curves move on the inside of the egg-tray rather than on the outside of the egg-tray, which appears to be the global minimum. This illustrates how *GEORCE* is guaranteed to converge to a local minimum and not a global minimum, and that this can be checked by expecting different initialization curves. For the sphere, there are infinitely many length-minimizing curves, and since we add the sign of a standard normal distributed variable for the random curves, we see that *GEORCE* tends to move in the direction of the closest local minimum.

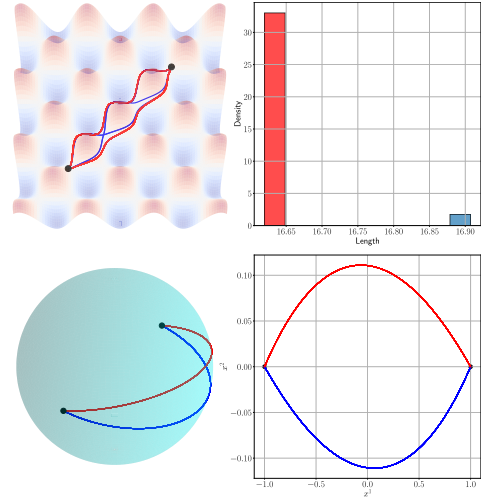


Fig. C1 The first row shows the estimated curves using *GEORCE* for the egg-tray, i.e. $f(x, y) = (x, y, 2 \cos x \cos y)$, while the second row shows the estimated curves for the sphere for different initializations of the initial curve.

Appendix D Manifolds

Table D1 contains a description of the Riemannian manifolds shown in the paper.

In the Finsler cases we consider a Riemannian manifold with a background metric, G , equipped with a force-field.

$$f(x) = \frac{\sin x \odot \cos x}{(\cos x)^\top G(x) \cos x},$$

where x denotes the local coordinates of the manifold. In this case the corresponding metric is a Randers metric, which is a special case of Riemannian metrics, of the form [51]

$$\begin{aligned} F &= \sqrt{a_{ij} \dot{r}^i \dot{r}^j} + b_i \dot{r}^i \\ a_{ij} &= g_{ij} \lambda + f_i f_j \lambda^2 \\ b_i &= -f_i \lambda \\ f_i &= g_{ij} f^j \\ \lambda^{-1} &= v_0^2 - g_{ij} f^i f^j, \end{aligned} \tag{D11}$$

where g_{ij} denotes the elements of the Riemannian background metric, f^j denotes the j th element of the force field, while v_0 denotes the initial velocity Riemannian length of an object moving with constant velocity v on the surface. For the manifold to be a proper Finsler manifold it is required that $\|f\|_g < v_0$.

Appendix E Variational autoencoders

E.1 Architecture

We train a Variational-Autoencoder (VAE) [52], where we use the normal distribution as a variational family to approximate the data distribution. We train a VAE for each of the following datasets

- MNIST data [56]: The data consists of 28×28 images of handwritten digits between 0 and 9. The data consists of 60,000 training images and 10,000 testing images.
- SVHN data [57]: The data consists of $32 \times 32 \times 3$ images of house numbers obtained through Google street view. The data consists of 73,257 digits for training and 26,032 digits for testing. We use approximately 80% of the training data for training similar to [12].
- CelebA data [53]: The data consists of 202,599 images of famous people of size $64 \times 64 \times 3$, where we use approximately 80% for training similar to [12].

The architectures for the VAE for MNIST data, SVHN data and CelebA data are shown in Table E2, Table E3 and Table E4, respectively. The architecture is similar to [12] with some modifications. All models are trained for 50,000 epochs on a GPU described in Appendix F.2.

E.2 Additional experiments

In Fig. E2 and Fig. E3 we show the geodesics between two reconstructed images using the learned VAE for the MNIST VAE and SVHN VAE, respectively, where we show the results using *GEORCE*, the initialization and alternative methods.

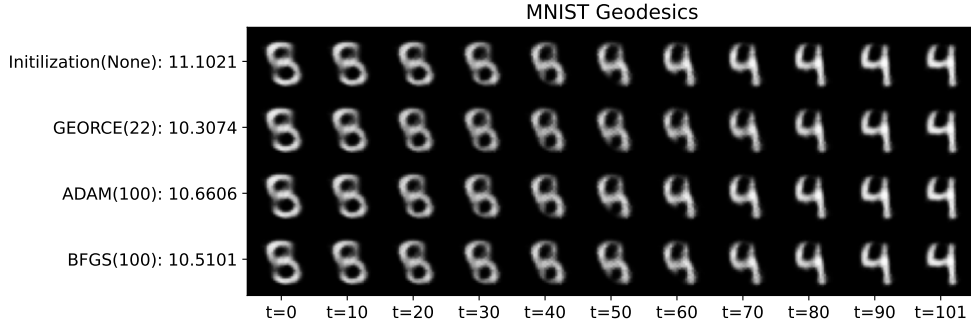


Fig. E2 The figure shows the results of using *GEORCE* and alternative methods for constructing geodesics for a Variational-Autoencoder [52] (VAE) for the MNIST dataset [56]. All algorithms are terminated if the ℓ^2 -norm of the gradient of the discretized energy functional in Eq. 5 is less than 10^{-3} , or if the number of iterations exceeds 100. We see that *GEORCE* uses less iterations and obtains the smallest length compared to the other algorithms. The details of the manifolds and experiments can be found in the supplementary material.

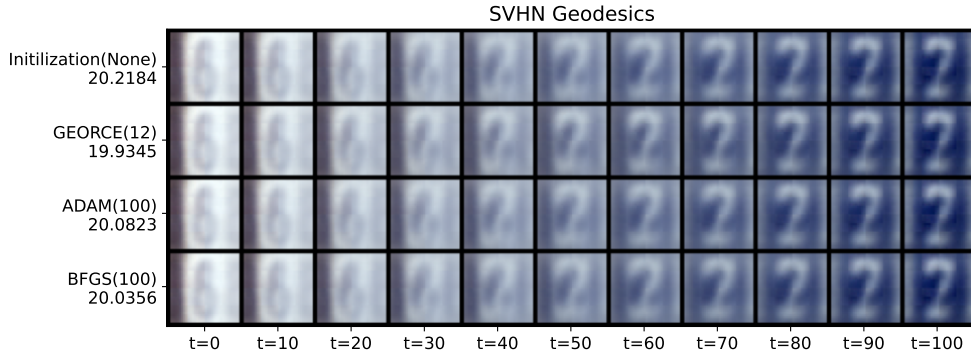


Fig. E3 The figure shows the results of using *GEORCE* and alternative methods for constructing geodesics for a Variational-Autoencoder [52] (VAE) for the SVHN dataset [57]. All algorithms are terminated if the ℓ^2 -norm of the gradient of the discretized energy functional in Eq. 5 is less than 10^{-3} , or if the number of iterations exceeds 100. We see that *GEORCE* uses less iterations and obtains the smallest length compared to the other algorithms. The details of the manifolds and experiments can be found in the supplementary material.

Appendix F Experiments

The following contains details of hyper-parameters, hardware and additional experiments. The implementation and code can be found at <https://github.com/FrederikMR/georce>.

F.1 Hyper-parameters and methods

Table F5 shows the hyper parameters used for the different methods. It is the same hyper-parameters that have been used for all manifolds across dimension and grid size in the paper.

Table F6 shows the integration methods used for solving the shooting problem.

All the timing estimates are computed by compiling the algorithms first, and then running the algorithm five times to compute the mean and standard deviation of the runtime. Table F7 states the start and end point of the geodesics constructed on the different manifolds in a local coordinate system as described in Table D1.

F.2 Hardware

All figures have been computed on a *HP* computer with Intel Core i9-11950H 2.6 GHz 8C, 15.6" FHD, 720P CAM, 32 GB (2×16GB) DDR4 3200 So-Dimm, Nvidia Quadro TI2000 4GB Discrete Graphics, 1TB PCIe NVMe SSD, 150W PSU, 8cell, W11Home 64 Advanced.

The runtime experiments on a CPU have been run on a CPU model *XeonE5_2660v3* with 1 nodes for at most 24 hours with a maximum memory of 10 GB.

The runtime estimates on a GPU and training of the VAE have been computed on a GPU for at most 24 hours with a maximum memory of 16 GB. The *GPU* consists of 1 node on a *Tesla V100*.

| Manifold | Description | Parameters | Local Coordinates |
|-----------------------|--|--|---|
| \mathbb{S}^n | The n-sphere, $\{x \in \mathbb{R}^{n+1} \mid \ x\ _2 = 1\}$ | - | Stereographic coordinates |
| $E(n)$ | The n-Ellipsoid, $\{x \in \mathbb{R}^{n+1} \mid \ p \odot x\ _2 = 1\}$ | Half-axes: $p = (0.5, \dots, 1)$ equally distributed points. | Stereographic coordinates |
| \mathbb{T}^2 | Torus | Major radius $R = 3.0$ and minor radius $r = 1.0$ | Parameterized by (θ, ϕ) with $x = (R + r \cos \theta) \cos \phi, y = (R + r \cos \theta) \sin \phi, z = r \sin \theta$. |
| \mathbb{H}^2 | 2 dimensional Hyperbolic Space embedded into Minkowski space \mathbb{R}^3 | - | Parameterized by (α, β) with $x = \cosh \alpha, y = \sinh \alpha \cos \beta, z = \sinh \alpha \sin \beta$. |
| $\mathcal{P}(n)$ | Paraboloid of dimension n | - | Parameterized by standard coordinates by $(x^1, \dots, x^n, \sum_{i=1}^n x_i^2)$ |
| $\mathcal{P}(n)$ | Symmetric positive definite matrices of size n^2 | - | Embedded into \mathbb{R}^{n^2} by the mapping $f(x) = l(x)l(x)^T$, where $l : \mathbb{R}^{n(n+1)/2} \rightarrow \mathbb{R}^{n \times n}$ maps x into a lower triangle matrix consisting of the elements in x . |
| 'Egg-tray' | A parameterized surface in shape of an egg tray | - | Parameterized by (x, y) with $x = x, y = y, z = 2 \cos x \cos y$. |
| Gaussian Distribution | Parameters of the Gaussian distribution equipped with the Fischer-Rao metric | - | Parameterized by $(\mu, \sigma) \in \mathbb{R} \times \mathbb{R}_+$. |
| Fréchet Distribution | Parameters of the Fréchet distribution equipped with the Fischer-Rao metric | - | Parameterized by $(\beta, \lambda) \in \mathbb{R}_+ \times \mathbb{R}_+$. |
| Cauchy Distribution | Parameters of the Cauchy distribution equipped with the Fischer-Rao metric | - | Parameterized by $(\mu, \sigma) \in \mathbb{R} \times \mathbb{R}_+$. |
| Pareto Distribution | Parameters of the Pareto distribution equipped with the Fischer-Rao metric | - | Parameterized by $(\theta, \alpha) \in \mathbb{R}_+ \times \mathbb{R}_+$. |
| VAE MNIST | Variational-Autoencoder equipped with the pull-back metric for MNIST-data | - | Parameterized by the encoded latent space. |
| VAE SVHN | Variational-Autoencoder equipped with the pull-back metric for SVHN-data | - | Parameterized by the encoded latent space. |
| VAE CelebA | Variational-Autoencoder equipped with the pull-back metric for CelebA-data | - | Parameterized by the encoded latent space. |

Table D1 Description of the manifolds used in the paper.

| Encoder | |
|---|------|
| Conv (output_channels = 64, kernel_shape = 4 × 4, stride = 2, bias = False) | GELU |
| Conv (output_channels = 64, kernel_shape = 4 × 4, stride = 2, bias = False) | GELU |
| Conv (output_channels = 64, kernel_shape = 4 × 4, stride = 1, bias = False) | GELU |
| Conv (output_channels = 64, kernel_shape = 4 × 4, stride = 2, bias = False) | GELU |
| Latent Parameters | |
| μ : Linear(out_feature = 8, bias = True), Identity | |
| σ : Linear(out_feature = 8, bias = True), Sigmoid | |
| Decoder | |
| Linear (out_feature = 50, bias = True) | GELU |
| Conv2dTransposed (output_channels = 64, kernel_shape = 4 × 4, stride = 2, bias = False) | GELU |
| Conv2dTransposed (output_channels = 32, kernel_shape = 4 × 4, stride = 1, bias = False) | GELU |
| Conv2dTransposed (output_channels = 16, kernel_shape = 4 × 4, stride = 1, bias = False) | GELU |
| Linear (out_feature = 784, bias = True) | |

Table E2 Architecture for VAE for the MNIST-dataset

| Encoder | |
|---|------|
| Conv (output_channels = 32, kernel_shape = 2 × 2, stride = 2, bias = False) | GELU |
| Conv (output_channels = 32, kernel_shape = 2 × 2, stride = 2, bias = False) | GELU |
| Conv (output_channels = 64, kernel_shape = 2 × 2, stride = 2, bias = False) | GELU |
| Conv (output_channels = 64, kernel_shape = 2 × 2, stride = 2, bias = False) | GELU |
| Latent Parameters | |
| μ : Linear(out_feature = 32, bias = True), Identity | |
| σ : Linear(out_feature = 32, bias = True), Sigmoid | |
| Decoder | |
| Conv2dTransposed (output_channels = 64, kernel_shape = 2 × 2, stride = 2, bias = False) | GELU |
| Conv2dTransposed (output_channels = 64, kernel_shape = 2 × 2, stride = 2, bias = False) | GELU |
| Conv2dTransposed (output_channels = 32, kernel_shape = 2 × 2, stride = 2, bias = False) | GELU |
| Conv2dTransposed (output_channels = 32, kernel_shape = 2 × 2, stride = 2, bias = False) | GELU |
| Conv2dTransposed (output_channels = 3, kernel_shape = 2 × 2, stride = 2, bias = False) | |

Table E3 Architecture for VAE for the SVHN-dataset

| Encoder | |
|---|------|
| Conv (output_channels = 32, kernel_shape = 4 × 4, stride = 2, bias = False) | GELU |
| Conv (output_channels = 32, kernel_shape = 4 × 4, stride = 2, bias = False) | GELU |
| Conv (output_channels = 64, kernel_shape = 4 × 4, stride = 2, bias = False) | GELU |
| Conv (output_channels = 64, kernel_shape = 4 × 4, stride = 2, bias = False) | GELU |
| Latent Parameters | |
| μ : Linear(out_feature = 32, bias = True), Identity | |
| σ : Linear(out_feature = 32, bias = True), Sigmoid | |
| Decoder | |
| Conv2dTransposed (output_channels = 64, kernel_shape = 4 × 4, stride = 2, bias = False) | GELU |
| Conv2dTransposed (output_channels = 64, kernel_shape = 4 × 4, stride = 2, bias = False) | GELU |
| Conv2dTransposed (output_channels = 32, kernel_shape = 4 × 4, stride = 2, bias = False) | GELU |
| Conv2dTransposed (output_channels = 32, kernel_shape = 4 × 4, stride = 2, bias = False) | GELU |
| Conv2dTransposed (output_channels = 3, kernel_shape = 4 × 4, stride = 4, bias = False) | |

Table E4 Architecture for VAE for the CelebA-dataset

| Method | Description | Parameters |
|----------------------------------|---|---|
| <i>GEORCE</i> | See algorithm in main paper | Backtracking: $\rho = 0.5$. |
| <i>ADAM</i> [40] | Moments based gradient descent method | $\gamma = 0.01$ (step size), $\beta_1 = 0.9$, $\beta_2 = 0.999$, $\epsilon = 10^{-8}$ |
| <i>SGD</i> [58] | Stochastic gradient descent | $\gamma = 0.01$ (step size), momentum=0, dampening=0, weight_decay=0. |
| <i>BFGS</i> [32–35] | Quasi-Newton method | - |
| <i>CG</i> [59] | Conjugate-Gradient method | - |
| <i>dogleg</i> [59] | trust region algorithm | - |
| <i>trust_ncg</i> [59] | Newton conjugate trust-region algorithm | - |
| <i>trust_exact</i> [59] | nearly exact trust region algorithm | - |
| <i>Sparse Newton</i> | See Appendix B.2 | Backtracking: $\rho = 0.5$. |
| <i>Sparse Regularized Newton</i> | See Appendix B.2 | Backtracking: $\rho = 0.5$ with $\lambda = 1.0$ and $\kappa = 0.5$. |

Table F5 The Hyper-parameters for estimating of the geodesics. We refer to Scipy [60] for the description and implementation of *BFGS*, *CG*, *dogleg*, *trust_ncg* and *trust_exact*.

| Method | Description | Parameters |
|--------------------|--|------------|
| <i>RK45</i> [61] | The explicit Runge-Kutta of order four to five | - |
| <i>RK23</i> [62] | The explicit Runge-Kutta of order two to three | - |
| <i>DOP853</i> [63] | The explicit Runge-Kutta of order eight | - |
| <i>Radau</i> [64] | Implicit Runge-Kutta method using Radau method | - |
| <i>BDF</i> [65] | Implicit multi-step order using backward differentiation | - |
| <i>LSODA</i> [66] | Method combining BDF and ADAM with stiffness detection | - |

Table F6 The ODE methods. The descriptions are from the *Scipy*-library [60].

| Manifold | Start point | End point |
|-----------------------|---|---|
| \mathbb{S}^n | n equally spaced points between 0 and 1 (end point is excluded) | $(0.5, 0.5, \dots, 0.5)$ |
| $E(n)$ | n equally spaced points between 0 and 1 (end point is excluded) | $(0.5, 0.5, \dots, 0.5)$ |
| \mathbb{T}^2 | $(0.0, 0.0)$ | $(5\pi/4, 5\pi/4)$ |
| \mathbb{H}^2 | $(1.0, 1.0)$ | $(0.1, 0.1)$ |
| Paraboloid | $(1, 1)$ | $(0, 0.5)$ |
| $\mathcal{P}(n)$ | The identity matrix in local coordinates | $n(n + 1)/2$ equally spaced points between 0.5 and 1.0. |
| 'Egg-tray' | $(-5.0, 5.0)$ | $(5.0, 5.0)$ |
| Gaussian Distribution | $(\mu_0, \sigma_0) = (-1.0, 0.5)$ | $(\mu_T, \sigma_T) = (1.0, 1.0)$ |
| Fréchet Distribution | $(\beta_0, \lambda_0) = (0.5, 0.5)$ | $(\beta_T, \lambda_T) = (1.0, 1.0)$ |
| Cauchy Distribution | $(\mu_0, \sigma_0) = (-1.0, 0.5)$ | $(\mu_T, \sigma_T) = (1.0, 1.0)$ |
| Pareto Distribution | $(\theta_0, \alpha_0) = (0.5, 0.5)$ | $(\theta_T, \alpha_T) = (1.0, 1.0)$ |

Table F7 The start and end point for the geodesics estimated for each manifold.